Research Square

Preprints are preliminary reports that have not undergone peer review.
They should not be considered conclusive, used to inform clinical practice,
or referenced by the media as validated information.

Promyelocytic Leukemia Protein Promotes Neuroprotection in a mouse model of Alzheimer's Disease by Modulating the Microglial Inflammatory Response

Syrago Spanou
FORTH Institute of Molecular Biology and Biotechnology
Takis Makatounakis
FORTH Institute of Molecular Biology and Biotechnology
Sofia Papanikolaou
Alexander Fleming Biomedical Sciences Research Center
Maria Protopapa
University of Crete
Ioanna Pandi
University of Crete
Elena Deligianni
FORTH Institute of Molecular Biology and Biotechnology
Dimitris Tzanos
FORTH Institute of Molecular Biology and Biotechnology
Christoforos Nikolaou
Alexander Fleming Biomedical Sciences Research Center
Panayiota Poirazi
FORTH Institute of Molecular Biology and Biotechnology
Joseph Papamatheakis
FORTH Institute of Molecular Biology and Biotechnology
Androniki Kretsovali
kretsova@imbb.forth.gr

FORTH Institute of Molecular Biology and Biotechnology

Research Article

Keywords: Promyelocytic Leukemia Protein (PML), Alzheimer's disease (AD), Amyloid beta, Microglia, Neuroinflammation

Posted Date: January 20th, 2026

DOI: https://doi.org/10.21203/rs.3.rs-8584272/v1

License: This work is licensed under a Creative Commons Attribution 4.0 International License.
Read Full License

Additional Declarations: No competing interests reported.

Version of Record: A version of this preprint was published at Journal of Neuroinflammation on October 23rd, 2026. See the published version at https://doi.org/10.1186/s12974-026-04088-4.

Abstract

Background

Alzheimer's disease (AD) is a progressive neurodegenerative disorder, characterized by amyloid deposition, neurofibrillary tangles, neuroinflammation and synaptic dysfunction. The Promyelocytic leukemia protein (PML) and the cognate nuclear bodies (PML-NB) have emerged as critical regulators of the nervous system, regulating neocortex development, neuronal survival, protein homeostasis and protection from stress. PML-NB have been implicated in the solubility of pathological aggregates in Neurodegenerative Diseases (NDD). However, the impact of PML on AD progression and whether its loss affects amyloid pathology remain unknown.

Methods

To investigate the role of PML in neuroinflammation we used intracerebroventricular (ICV) injections of oligomeric amyloid beta 1–42 ($oA\beta_{1-42}$), in WT and *Pml-/-* mice and primary microglia cultures derived from these genotypes. To explore the role of PML in AD pathology we employed phenotypic, transcriptomic and behavioral analyses of WT, *Pml-/-*, 5xFAD and 5xFAD *Pml-/-* mice.

Results

Pml-/- mice displayed reduced recruitment and activation of microglia in the vicinity of $oA\beta_{1-42}$ injection, accompanied by deregulated expression of disease-associated microglia (DAM) genes. Consistently, Pml-/- primary microglial cultures exhibit reduced phagocytosis, activation, viability and impaired cytokine responsiveness following β-amyloid challenge. PML depletion in 5xFAD mice accelerates Aβ accumulation, impairs microglial activation, lysosomal acidification and recruitment to amyloid plaques while enhances astrocyte reactivity and neuronal degeneration. Hippocampal transcriptomic analyses reveal sex-dependent effects of PML loss, with downregulation of pathways related to cell migration, axonogenesis and synapse organization in 5xFAD *Pml-/-* females and peroxisomal functions, DNA repair and immune responses, in 5xFAD *Pml-/-* males. Both sexes show suppression of immune response genes and deregulated expression of DAM genes. PML depletion increases impulsivity and hippocampus-dependent behavioral abnormalities in the context of Aβ pathology, highlighting a role for PML in maintaining cognitive function.

Conclusions

PML loss exacerbates multiple aspects of AD pathophysiology including amyloid deposition, impaired anti-inflammatory responses, neurotoxicity and cognitive performance. Our findings identify PML as a key regulator for microglial homeostasis and neuroprotective functions in amyloid pathology. Through its

actions in microglia, PML emerges as an effector and a marker of aging and neurodegeneration. Restoring or enhancing its activity may represent a promising therapeutic strategy to preserve neuronal function in AD.

1. Background

Alzheimer's disease (AD) is a progressive multifactorial neurodegenerative disorder, estimated to account for 60%–70% of all dementia cases worldwide [1]. AD pathology is characterized by the accumulation of amyloid-β (Aβ) plaques in the brain parenchyma, intra-neuronal aggregation of hyperphosphorylated-TAU protein, vascular alterations, neuroinflammation and synaptic dysfunction, ultimately leading to neuronal loss and cognitive decline [2, 3]. The "amyloid hypothesis" has long suggested that Aβ deposition drives AD pathogenesis and neurodegeneration [4]. Genetic evidence demonstrating that dominant mutations causing early onset AD occur in genes coding either for the amyloid precursor protein (APP) or its processing enzymes (presenilin 1 and 2), and leading to Aβ build-up, further supported this hypothesis [5, 6]. Recent evidence shows that Aβ aggregation triggers glial responses, myelin damage and neurotoxicity, marking the cellular phase of AD [3]. The multicellular network in the plaque niche drives neuroinflammation and the manifestation of cognitive deficiency [3]. Genome-wide association studies (GWAS) have identified several genetic variants as AD risk factors [7, 8], linked to immune-related pathways and highly expressed in microglia, including TREM2, CD33, INPP5D, PLCG2, BIN1, and PICALM [9, 10],

Microglia, the tissue-resident macrophages of the brain parenchyma, derive from erythromyeloid progenitor cells in the embryonic yolk sac and colonize the brain early during embryonic development [11]. They play key roles in immune surveillance, by clearing pathogens, dead cells and protein aggregates, including Aβ plaques, thus maintaining tissue homeostasis [12, 13]. Beyond immune functions, microglia are critical in brain development and circuit refinement, regulating synaptic pruning and neuronal plasticity, functions that require metabolic flexibility [14, 15][16]. In neuroinflammatory conditions, such as AD, microglia act as primary damage sensors of the CNS. They are recruited to Aβ plaques where they proliferate, engulf Aβ peptides through phagocytosis and secrete cytokines, including type I interferons [17], interleukin-1β [18] and tumor necrosis factor-α [19]. Upon amyloid plaques recruitment, microglia adopt an activated morphology and exhibit disease-associated microglia (DAM) transcriptional signatures, that include upregulation of genes such as *Trem2*, *Tyrobp*, and *Apoe* and downregulation of homeostatic genes [20–22]. The transition to a neuroprotective DAM phenotype is TREM2-dependent [20–22]. In addition, microglia exhibit heterogeneity and are composed of subpopulations with diverse functional signatures that may account for distinct roles during AD progression [23–25].

The promyelocytic leukemia protein (PML) initially identified as a tumor suppressor, is the core organizer of PML-nuclear bodies (PML-NBs) that regulate diverse biological processes such as anti-viral responses, gene expression, stem cell renewal, apoptosis and metabolism [26]. In the nervous system, PML regulates brain development, circadian rhythm and synaptic plasticity [27]. In the immune system,

PML is induced by diverse stimuli including type I and II interferons and regulates both innate and adaptive immunity by enhancing IFN signaling through interactions with STAT1 and STAT3 [28]. Further, it enhances transcription of interferon stimulated genes (ISGs) [29]. Interestingly, PML induction by interferon β occurs not only in immune, but also in neural cells [30]. PML deficiency impairs the innate immune responses to *Listeria monocytogenes* infection in mice, causing spontaneous granulomatous lesions due to defective macrophage function [31].

PML has been shown to exert neuroprotective effects during early cerebral ischemia, highlighting its role in both protection and recovery [32]. PML also degrades mutant ataxin-7, alleviating neurodegeneration in spinocerebellar ataxia-7 models [30, 33, 34]. Furthermore, PML-NBs decline with age [35] and are significantly reduced in hippocampal neurons of ALS-FTD patients [36], suggesting that PML plays a key role in maintaining CNS homeostasis and regulating neurodegeneration mechanisms. However, the involvement of PML in AD has not been explored.

Previously, we demonstrated that PML protects mouse embryonic neural stem cells (eNSC) from amyloid stress induced cell death and safeguards proteostasis by enhancing both autophagy and proteasomal functions. In addition, PML sustains eNSC mitochondrial integrity by supporting the activities of PGC-1α and the PPARγ pathways [37].

In this study, we addressed the role of PML in neuroinflammation and amyloid pathology in animal models of AD. By combining intracerebroventricular injections of oligomeric amyloid beta 1–42 ($oA\beta_{1-42}$) in wild-type and *Pml-/-* mice, along with comparative analysis of phenotypic, behavioral and RNA sequencing studies in 5xFAD, *Pml-/-* and 5xFAD *Pml-/-* mice, we uncovered a novel function of PML that acts as a protective factor in the context of AD pathology. Our results demonstrate that PML-deficient microglia show impaired reactivity to Aβ plaques, reduced survival, deregulated cytokine signaling and defective phagocytosis, contributing to neuronal degeneration. The ablation of PML aggravates multiple aspects of 5xFAD pathophysiology including amyloid deposition, microglial deficiency, neurotoxicity and deterioration of cognitive functions. Taken together, our findings identify PML as an essential mediator for microglial homeostasis and neuroprotective functions, in amyloid pathology.

2. Materials & Methods

Mice

C57BL/6 control (WT), 5xFAD (stock #034848-JAX) and C57BL/6-$Pml^{tm1(PML/RARA)Ley}$/J (*Pml-/-*) (stock #017959-JAX) mice were obtained from the Jackson Laboratory. 5xFAD mice were maintained as heterozygotes through mating them with C57BL/6 J. For 5xFAD *Pml-/-* studies, *Pml-/-* mice were crossed to 5xFAD to obtain heterozygous 5xFAD *Pml+/-*, which were further crossed to *Pml-/-* to generate 5xFAD *Pml-/-* littermates. Mice were genotyped using polymerase chain reaction (PCR) before experiments. Only male mice were used for functional experiments and both females and males for RNA-sequencing

and amyloid deposition analysis, as described in figure legends. Mice were housed, bred and treated at the IMBB animal facility according to standard animal welfare practices. All animals were housed in appropriate cages with 12 h dark and 12 h light cycle, ambient temperature, humidity and ad libitum access to food and water. The IMBB animal facility operates in compliance with the “Animal Welfare Act” of the Greek government, using the “Guide for the Care and Use of Laboratory Animals” as its standard (Facility license: EL 91 BIObr 01, EL 91 BIOexp 02). All procedures were conducted according to Greek national legislations and institutional policies following approval by the FORTH ethical committee. Procedures used for the current studies were approved by the General Directorate of Veterinary Services, region of Crete (license numbers: 184380, 90851).

Primary microglial culture preparation

To examine microglia viability, activation and phagocytosis, mixed glial cell cultures were established from the cortices of postnatal day 2 (P2) WT and *Pml-/-* pups, as previously described [38]. Briefly, cortices were dissected under sterile conditions and meninges were carefully removed. Tissues were enzymatically dissociated in 0.025% trypsin for 10min at 37°C, followed by gentle trituration. Cell suspensions were plated in poly-D-lysine (0.01 mg/ml PDL, Sigma-Aldrich)-coated 75cm2 culture flasks, containing DMEM (GlutaMAX™, 4.5 g/L d-Glucose, -Pyruvate, Gibco), supplemented with 10% FBS (Gibco) and 0.05mg/ml Gentamycin. Cultures were maintained at 37°C in a humidified 5% CO_2 incubator and the medium was replaced twice weekly. After 14 days *in vitro*, when a clear, confluent layer of cells was formed, the mixed glial culture was separated into different cell populations according to their ability to attach to the flask. Microglial cells were detached from the astrocytic monolayer by orbital shaking at 200 rpm for 1 h at 37°C. The culture medium containing detached microglia was collected and centrifuged at 300 g for 10 min. Cell pellets were resuspended in completed DMEM and seeded at a density of $15x10^4$ cells/ml on PDL-coated glass coverslips. Microglial cells were allowed to adhere overnight, then serum-starved (DMEM supplemented with 0.1% FBS and 1% gentamycin) for 4 h prior to Aβ treatment. Cells were subsequently treated with $oA\beta_{1-42}$ 1 and 5μM, for 48h to induce microglial activation or assess cell viability. Following treatment, cell culture supernatants were collected and stored at − 80°C for subsequent ELISA analysis.

To examine antigen presentation functions of pathological microglia, primary microglia were isolated from whole brains of 6-month old WT, *Pml-/-*, 5xFAD and 5xFAD *Pml-/-* mice. Brains were rapidly excised and washed in ice cold DMEM (Gibco) supplemented with 10% FBS(Gibco) and 0.05mg/ml gentamycin. Tissues were minced and enzymatically dissociated in 1 mg/ml collagenase type IV for 40min, at 37°C. The enzymatic reaction was terminated by adding complete medium and cell suspensions were centrifuged at 280xg for 5 min. Cells were resuspended in fresh DMEM and dissociated using a syringe (21G needle), followed by filtration through a 40μm cell strainer to remove debris and aggregates. Next, myelin and cellular debris were removed by density gradient centrifugation using isotonic Percoll solutions. Briefly, cell pellets were resuspended in 3ml of 75% Percoll isotonic solution, overlaid with 5 ml 35% Percoll and topped with 1 mL of ice-cold 1xPBS. Gradients were centrifuged at 800xg for 40 min at 4°C, with no brake. The interphase containing microglia, was carefully collected, diluted in 1xPBS and

centrifuged at 300xg for 5 min. Microglial cells were then prepared for immunostaining and flow cytometry analysis.

Intracerebroventricular injections (ICV)

Three-month-old WT and *Pml-/-* mice were anesthetized with ketamine (100 mg/kg)/xylazine (10 mg/kg) and kept on a thermal blanket in a stereotaxic frame (Stoelting). Under aseptic conditions, an incision along the midline was made to reveal the skull and craniotomies were drilled with a 005 carbide drill round (Hager & Meisinger GmbH) to allow bilateral injections into the lateral ventricles. Pulled long-shaft glass pipettes (Drummond) were backfilled with mineral oil before loading oAβ_{1-42} (250nM) or sterile 1xPBS vehicle. Next, four microliters total volume was injected into both lateral ventricles in the following coordinates: -0.5mm anterior/posterior, -2.3mm dorsal/ventral and ± 1.0mm lateral from bregma (Paxinos and Franklin's the Mouse Brain in Stereotaxic Coordinates, Fourth Edition), using an ultra-precise digital mouse stereotaxic instrument (Stoelting) at a flow rate of 0.3 µl/min. After completing the injections, the pipette was kept in place for 5 min and then slowly withdrawn to avoid backflow. Carprofen (5 mg/kg) was administered subcutaneously after the surgery. Upon completion of injections, mice were allowed to wake up from anesthesia. No signs of pain, distress or other behavioral changes were observed during or after the procedure. 72 h after ICV injections, mice were sacrificed and brains were harvested for immunohistochemistry and RT-qPCR analysis.

Immunostaining

Mice were anesthetized by intraperitoneal injection with a ketamine/xylazine mixture (1:1) and then transcardially perfused using 1xPBS. Brains were removed and separated in hemispheres. The right hemisphere was fixed in fresh 4% paraformaldehyde (PFA) for 48h at 4 C, while cortices and hippocampi from the left hemispheres were dissected and stored at − 80°C for subsequent protein and RNA analyses. Post fixation, hemispheres were washed twice with 1× PBS, then transferred to 30% sucrose for cryoprotection for 48h at 4°C, embedded in 7.5% gelatin–15% sucrose and rapidly frozen in a dry ice isopentane bath. 20µm coronal cryosections were mounted on Superfrost Plus microscope slides (Thermo) and stored at − 80°C until further use. Cryosections were permeabilized in ice-cold acetone at − 20°C for 4 min, followed by washes in 0.1% Triton X-100 in 1× PBS for 15 min and 0.3% Triton X-100 in 1x PBS for 30 min, at room temperature (RT). Sections were blocked in 10% goat serum (Abcam) containing 0.1% Triton X-100 in 1× PBS and 0.1% BSA for 1 hr RT and then incubated with primary antibodies (**Table S.1**), diluted in blocking solution overnight at 4 C. The following day, slides were washed three times (15 min each) in 0.1% Triton X-100 in 1× PBS and incubated with the appropriate fluorochrome-labeled secondary antibodies for 1 h, RT (**Table S.1**). Sections were again washed three times for 15 min as before and cell nuclei were visualized with DAPI. For Thioflavin S staining, sections were stained with 1% Thioflavin S (ThioS) (Sigma-Aldrich) solution in 50% ethanol for 8min RT, followed by three washes with 50% ethanol for 2 min and one wash with 1xPBS. Slides were covered with Mowiol® 4–88 mounting medium. For each condition, at least three tissue sections per animal were analyzed and three or more animals were included per genotype, as indicated in the figure legends. For

immunofluorescence experiments in primary microglia, cells were fixed in 4% PFA for 20 min, permeabilized with 0.5% Triton-X in 1× PBS for 5 min and blocked with 1% BSA for 1h, RT. After incubation with primary antibodies for 1 h at RT, secondary fluorescent antibodies were added for 1h and DAPI or TO-PRO-3 were used for nuclear counterstaining. All samples were imaged with a Leica SP8 inverted confocal laser scanning microscope, equipped with 40X and 63X oil objectives and analyzed with Fiji (ImageJ) software.

Confocal imaging and analysis

All samples including brain cryosections and primary microglia were analyzed using a Leica SP8 inverted confocal laser scanning microscope, equipped with 40X and 63X oil objectives. All images were acquired with the same image acquisition settings to ensure consistency across experiments. A z-step size of 0.5 µm step size for *in vitro* microglial cultures and 0.7µm step size for brain sections, at 1024 x 1024 pixels. For quantification analyses, identical laser intensities and z-stacks with same number of sections were used, for all conditions within experiments, using the Fiji software. Densitometric analyses were used for the quantification of PML, IBA1, glial fibrillary acidic protein (GFAP), TREM2 and cleaved-caspase-3 immunohistochemistry. Channels were split and regions of interest (ROIs) were manually designed with a free-hand tool for distinct hippocampal regions (DG, CA1, CA3) and the restrosplenial cortex (RSC). For TREM2 fluorescent intensity measurements in microglial cultures, channels were split and regions of interest (ROIs) were designed with a free-hand tool. The mean fluorescent intensity (MFI) was calculated by subtracting the MFI of a non-fluorescent area (background ROI) from the MFI of the fluorescent signal. To evaluate microglial Aβ engulfment, three-dimensional (3D) segmentations of Aβ plaques were generated for ThioS and CD68 stainings in Fiji, as described previously [39]. Threshold was applied and binary masks were created. Using the 3D object counter plugin in Fiji (Image J), the volume of ThioS mask (plaque volume) and the intersection of CD68 and ThioS volume (engulfed volume) was calculated for each plaque. A minimum of 15 individual plaques per brain section were analyzed from 3 sections per mouse and four animals in total were examined per genotype. Microglial morphology was analyzed using the skeletonize (2D/3D) analysis plugin in Fiji (Image J). IBA1 + microglia were binarized, thresholded and then skeletonized to quantify the number of branches, junctions, triple and quadruple points per cell. Sholl analysis was also performed on the same cells. A radius was drawn from the center of the cell soma to the end of the cell. The first circle was positioned close to the cell body and the distance between each circle was set at 3 µm for all cells. The number of times that the microglial branches intercepted each circle was calculated with Fiji (ImageJ) software.

Western blot analysis (WB)

Frozen brain hemispheres were thawed on ice and mechanically homogenized using a tissue homogenizer in RIPA buffer (1% Triton, 50 mM Tris pH 7.6, 150 mM NaCl, 0.5% deoxycholate, 1mM EDTA, 1 mM PMSF, 20% glycerol) supplemented with protease phosphatase inhibitor cocktail (Complete EDTA Free; Roche Applied Science). Protein concentration was determined by Bradford assay and equal amounts of proteins (40 µg) were subjected to SDS/PAGE, as previously described [37]. Samples were

then transferred to nitrocellulose membrane (Amersham Hybond), blocked with 5% BSA in TBST, followed by immunoblotting. The SuperSignal West Pico PLUS Chemiluminescent Substrate (Thermo) was used to detect signal by ChemiDoc Imaging System (Biorad). The primary and secondary antibodies used for WB are listed in **Table S.1**

ELISA

To quantify the ratio Aβ42/40 in both soluble and insoluble fractions, brain hemispheres were used. Samples were mechanically homogenized in lysis buffer and centrifuged at 15,000rpm for 20min at 4°C. Supernatants were collected as soluble fractions. For the insoluble fraction, brain homogenate pellets underwent guanidine extraction. Pellets were incubated in 5 M Guanidine HCl/50 mM Tris (pH = 8.0) solution at a 1:5 ratio, for 3hr RT and further diluted 1:5 in PBS containing protease inhibitors. Samples were then centrifuged at 15,000rpm for 20min at 4°C and supernatants (insoluble fraction) were stored at − 80°C until analysis. The protein concentrations of soluble and insoluble fractions were determined by Bradford assay. Both fractions were further diluted for ELISA. Human amyloid beta (1–42) LEGEND MAX (Biolegend, #448707) and human amyloid beta (1–40) LEGEND MAX (Biolegend, # 449007) ELISA kits were used for standard curves and assay was performed according to manufacturer's instructions. To measure TNF-α and IL-10 levels in microglial culture supernatants, mouse TNF-α LEGEND MAX (Biolegend, #431417) and mouse IL-10 LEGEND MAX (Biolegend, #430907) ELISA kits were used for standard curves and assays were performed according to manufacturer's instructions. Absorbance was measured at 450nm using a Berthold Apollo microplate absorbance reader.

Flow cytometry

Single-cell suspensions obtained after Percoll density gradient centrifugation were resuspended in 100 µL 1xPBS/5% FBS and stained with fluorochrome-conjugated antibodies for 30 min at 4^{o}C, in the dark. The following antibodies were used: CD11b-APC (1:100), CD45-PE (1:100), MHC-II-FITC (1:100) and CD86-PerCP (1:100). For lysosomal activity assessment cells were incubated with 1µM LysoSensor™ Green DND-189 (Invitrogen, L7535) diluted in warm DMEM for 45 min at 37^{o}C. Following staining, cells were washed with 1xPBS/5% FBS at 400g for 5min. Cell analysis was performed using a BD FACSAria™ Fusion flow cytometer (BD Biosciences). For the gating strategy, FSC/SSC was initially applied to exclude debris and select viable cells (alive cells) and FSC-A/SSC-A was then applied to remove doublets. Microglia were identified as CD11b^{+}CD45^{int}cells and median fluorescence intensity (MFI) for MHC-II, CD86 and lysosensor was quantified. Data were analyzed using FlowJo software (Tree Star).

In vitro phagocytosis assay

Primary microglia from WT and Pml-/- mice were seeded on PDL coated 8mm glass coverslips at a concentration of 15x10^{4} cells/ml and cultured in growth medium at (incubator conditions). The next day Fluoresbrite® BB Carboxylate Microspheres 1.75µm (Polysciences) 15x10^{3} beads/ml were added in microglial cultures and incubated for 1.5, 3 and 6 hours at 37^{o}C. To examine phagocytosis of microglial

cells, coverslips were then washed with PBS to remove noninternalized beads, fixed with fresh 4% PFA for 20 min, at RT and stained for IBA1 and TO-PRO3, as previously described. Cells were imaged with a Leica SP8 inverted confocal laser scanning microscope, using a 63X oil objective and analyzed with Fiji (ImageJ) software.

Celltox assay

Celltox assay (Promega) was used to evaluate primary microglia survival according to the manufacturer's instructions. Primary microglial cells were cultured for 48 h in proliferation medium (containing 10% FBS) and subsequently treated with oligomeric amyloid-β (1–42) 1 μM and 5 μM (AnaSpec), for 48 h in serum free conditions. The stock solutions of amyloid-β was dissolved in 1× PBS according to the manufacturer's instructions. The same volume of 1× PBS was added to the controls of each experiment. Celltox and Hoechst (1:10,000, Invitrogen) were added to each well simultaneously with the amyloid treatments. Cells were imaged with a Leica Led Inverted fluorescent microscope and analyzed with Fiji (ImageJ) software.

High content screening image processing and analysis

Hippocampal sections from 5xFAD and 5xFAD *Pml-/-* 6month old mice were stained for amyloid plaques and were imaged on a high-content Operetta microscope (Perkin Elmer), using a 20x objective lens. For quantification and analysis, amyloid deposits were segmented based on the green fluorescence channel and selected according to defined morphological and intensity criteria. Analysis was based on the Harmony 4.1 software (Perkin Elmer). Because the software could not reliably delineate the borders of distinct brain regions, this step was performed manually. All acquired images were tiled to generate a comprehensive map of each brain section, and regional differentiation was guided by reference to the Paxinos and Franklin's mouse brain atlas (Fourth Edition). Subsequently, amyloid deposits were manually identified, while all quantitative parameters were extracted automatically using the analysis algorithm.

Mouse behavioral tests

For all behavioral experiments, 6-month-old male mice were used and tested during the dark phase of a 12 h light/dark cycle. The object location (OL) task and open field test (OFT) were evaluated in a square open-field arena (35 × 40 × 35 cm) made of plexiglas, to assess spatial object memory and exploratory and anxiety-like behavior, respectively [40]. Before the test, mice were handled twice for four days, with 3 hours apart. After handling, the habituation lasted two days before the test, with 10 minutes of each session. During habituation, mice activity was recorded, evaluating, among others, stereotypical jumping behavior. The test began with the sample phase, in which mice were placed in the arena and allowed to explore two identical objects for 10 minutes. After a 3h retention delay, mice underwent a 2-minute choice phase. During this phase, one object from the sample phase and one novel object, were presented. The object from the sample phase was transferred to an adjacent corner of the arena during the choice phase, making its position rather than its identity, the novel element. The order of object pairs, the designated sample and novel objects within each pair and the side of the apparatus (left or right) on

which the novel object was placed during the choice phase, were all counterbalanced. Novelty preference was quantified by calculating a discrimination index (DI) defined as: DI = (novel object exploration – familiar object exploration)/(total object exploration). In the sample phase, both objects were equally novel, and a DI of approximately zero was expected. In the choice phase, a DI significantly greater than zero indicated novelty preference, which was interpreted as evidence of intact memory. Mice activity was recorded using an overhead video camera and (Logitech) analyzed using Smart v3.0 video tracking software (Panlab). Outliers (> 2 S.D from the mean) and mice that spent less than 3% of the sample phase exploring, were excluded from analyses.

RNA isolation and quantitative real-time PCR (RT-qPCR)

Total RNA was extracted from hippocampi or microglia using Nucleozol (Macherey-Nagel) according to the manufacturer's instructions, as previously described [37]. In brief, RNA concentration was determined using a NanoDrop 2000 spectrophotometer (Thermo Fischer Scientific) and 1µg RNA was reversely transcribed to cDNA by M-MuLV Reverse Transcriptase (NEB) supplemented with RNase inhibitor (NEB) according to the manufacturer's protocol. Quantitative RT-PCR was carried out using Luna Universal qPCR Master Mix (NEB) and Biorad CFX96 Touch Real-Time PCR Detection System. Gene expression levels were normalized to β-Actin and F4/80 for microglial genes. Primer sequences used for qRT-PCR are presented in **Table S.2**

3' RNA sequencing

The RNA samples were analyzed using Agilent RNA 6000 Nano kit with the bioanalyzer from Agilent. RNA samples with RNA integrity number (RIN) > 7 were used for library construction using the QIAseq UPX 3' Transcriptome kit (QIAGEN 333088), starting with 10 ng of total RNA and relying on UPX tagging for samples multiplexing and UMIs for accurate gene expression as per the manufacturer's instruction (QIAGEN Cell ID 25–48). We examined the hippocampus of WT, *Pml-/-*, 5xFAD and 5xFAD *Pml-/-* mice (3 males and 3 females per group). Amplification was controlled for obtaining optimal unbiased libraries across samples (13 + 8 cycles). DNA High Sensitivity Kit for bioanalyzer was used to assess the quantity and quality of libraries, according to the manufacturer's instructions (Agilent). Libraries were sequenced on an Illumina Nextseq 2000 (paired end with 101 cycles read 1, 12 cycles index 1 and 50 cycles read 2) at the genomics facility of IMBB-FoRTH according to the manufacturer's instructions and the number of reads obtained for each sample after demultiplexing and the percentage of reads aligning to mm10 genome are listed in **Table S.3.**

Differential Expression Analysis (DEA) and Gene Ontology (GO) enrichment analysis of bulk RNA sequencing data

The quality of the raw sequences in output FASTQ files was assessed with the FastQC software. A detailed description of the process is provided in **supplementary material 1.** Differential gene expression analysis was performed using DESeq2. Genes were included in the analysis if they exhibited an average

normalized count of at least 5 across all samples. For comparisons among the four experimental conditions (WT, *Pml-/-*, 5xFAD and 5xFAD *Pml -/-*), sex was accounted for as a covariate in the model design. In addition to the combined analysis, differential expression was also assessed separately within each sex. Differentially expressed genes (DEGs) in either group of the comparison, were defined by applying the following thresholds |Log2FC| >0.58 and p-adj < 0.05, which was considered statistically significant.

Statistical analysis

All statistical analyses and graphs were performed using the GraphPad Prism 8.0.2 software. All graphs represent values as mean and the standard deviation (mean ± SD), as indicated in the figure legends. The p-value < 0.05 was considered significant difference, determined by unpaired t-test, one-way or two-way ANOVA comparisons, as indicated in the figure legends. *p < 0.05, **p < 0.01, ***p < 0.001, ****p < 0.0001, n.s (not significant). Experiments were repeated at least 3 times. For animal studies, each biological replicate consisted of 3–6 mouse tissues or cell cultures per genotype per time point or treatment. Quantification of fluorescence microscopy, confocal microscopy and high content images were performed using the Fiji (ImageJ) or the Harmony high-content imaging software (PerkinElmer).

3. Results

3.1. PML expression changes with the progression of amyloid pathology in 5xFAD mice

Recent reports indicate that PML supports the health of neural stem cell (NSC) by preserving proteostasis and mitochondrial integrity, thereby preventing the accumulation of misfolded proteins [37]. To investigate whether PML plays a role in the pathology of Alzheimer's disease (AD), we first examined the expression of PML in the 5xFAD mouse model of familial AD. 5xFAD mice exhibit robust amyloid deposits starting from 2 months, neuronal loss and gliosis accompanied by cognitive deficits starting at 4–6 months [41]. We stained brain cryosections from the prefrontal cortex and the hippocampus of 2 and 6-month old wild-type mice and found that PML is expressed in the nucleus of MAP2 + neurons and in the branches of homeostatic microglia **(**Fig. 1A**)**. Conversely, in 5xFAD mice the nuclear expression of PML was decreased at both the 2 and 6-month time points and mainly expressed in reactive microglia **(**Fig. 1A**)**. We proceeded to examine PML expression in the course of amyloid pathology from 2 to 12 months, focusing on the hippocampus and the restrosplenial cortex (RSC). Concordantly with the increase of the glial marker IBA-1, we observed a significant reduction of PML expression in 2-month-old mice in the dentate gyrus (DG), CA1 and CA3 **(**Fig. 1B, C **and Fig. S1A-D)**, but not in the RSC **(**Fig. 1D, E**)**. Furthermore, as amyloid deposits increased, we observed that PML nuclear expression declined and was enriched in microglia surrounding amyloid plaques. Interestingly, we also detected reduced PML expression in aged WT animals (6 months and 12-months), in the hippocampus but not in the RSC. Taken together, these results suggest that PML reduction is an early event in brain regions susceptible to amyloid pathology and possibly implicated in age-dependent processes.

3.2. PML regulates neuroinflammation induced by amyloid β challenge

Our initial observation that PML expression is enhanced in reactive microglia during amyloid pathology, led us to hypothesize that it could participate in molecular mechanisms regulating neuroinflammation. To investigate the contribution of PML in neuroinflammation, we established an acute neuroinflammation model in WT and *Pml-/-* mice. We administered oligomeric $A\beta_{1-42}$ ($oA\beta_{1-42}$) via intracerebroventricular injections (ICV) in both lateral ventricles (250nM/ ventricle, M/L 1mm, A/P -0.5mm, D/V -2.3mm) of 6–8 weeks old WT and *Pml-/-* mice and studied microglia responses in the hippocampus **(**Fig. 2A**)**. 72 hours post injection we harvested brain tissues for further examination. Densitometric analysis of immunohistochemistry data revealed that *Pml-/-* mice injected with $oA\beta_{1-42}$, showed decreased expression of IBA-1 + activated microglia in distinct areas of the hippocampus (DG, CA1 and CA3), compared to $oA\beta_{1-42}$ injected WT mice **(**Fig. 2B, C**)**. No significant microglia reactivity was observed in WT and *Pml-/-* mice, injected with PBS as negative controls **(**Fig. 2C **and Fig. S2A)**. Furthermore, *Pml-/-* mice injected with $oA\beta_{1-42}$ displayed increased neuronal apoptosis, as indicated by elevated levels of cleaved caspase-3 in MAP2 + neurons of the hippocampus and RSC, compared to WT mice **(Fig. S2B, C)**. These results show that impaired recruitment and activation of microglia in the vicinity of $oA\beta_{1-42}$ injection sites may contribute to increased neurotoxicity in *Pml-/-* hippocampi.

RT-qPCR analysis revealed increased *Pml* expression in WT mice, in response to Aβ administration **(**Fig. 2D**)**, suggesting that PML is required for immune responses to amyloid oligomers in the hippocampus. To test this possibility, we examined the expression of genes associated with inflammation and found that $oA\beta_{1-42}$ injected *Pml-/-* mice showed decreased expression of *Interleukin-1b*, increased *Nos2* and markedly decreased expression of anti-inflammatory genes (*Interleukin-4*, *Interleukin-10*, *Arginase 1*), compared to $oA\beta_{1-42}$ injected WT mice **(**Fig. 2E**)**. Furthermore, we examined how microglia respond transcriptionally to Aβ by evaluating the expression of specific disease-associated microglia (DAM) genes [10, 21]. WT hippocampi showed increased expression of DAM genes following $oA\beta_{1-42}$ injection **(**Fig. 2F **and Fig. S2D)**, confirming microglial activation. Conversely, in $oA\beta_{1-42}$ injected *Pml-/-* mice, we detected significantly reduced expression of several DAM genes, including the neuroprotective factor *Trem2*, *Cst7* and *Spp1* **(**Fig. 2F **and Fig. S2D)**. In contrast, the expression of *Apoe* **(**Fig. 2F**)** and *Siglec-3* **(Fig. S2D)**, which associate with AD risk [10, 42], was increased in correlation with decreased *Trem2* [43]. Collectively, these data support an essential role of PML in mediating the innate immune responses of microglia to $oA\beta_{1-42}$ in the hippocampus.

Activated microglia undergo distinct morphological and functional transformations. Due to their pronounced plasticity, they can expand, migrate and transition from a highly ramified to an amoeboid morphology and gain enhanced phagocytic capacity, by high expression of IBA-1. In order to determine the cellular and molecular mechanisms underlying the $oA\beta_{1-42}$ effects on the activation of microglia in the absence of PML, we established *in vitro* primary microglial cultures derived from postnatal day 2 (P2)

WT and *Pml-/-* mouse pups. We incubated WT and *Pml-/-* microglia to buffer alone or 1μM oAβ_{1-42} for 48 hours and observed increased expression of TREM2 in WT as opposed to *Pml-/-* cultures relative to untreated controls **(**Fig. 3A, B**)**. Cell viability assays (CellTox) revealed that *Pml-/-* microglia exhibited increased cell death after 48h treatment with 1 or 5 μM oAβ_{1-42}, in comparison to WT microglia counterparts **(**Fig. 3C **and Fig. S3A)**. Of note, in starvation relative to control conditions (1% vs 10% FBS respectively), *Pml-/-* cells showed higher baseline mortality, suggesting a pro-survival role of PML under stress conditions[37] **(**Fig. 3C **and Fig. S3A)**. To further evaluate microglia status after treatment with oAβ_{1-42}, supernatants from microglial cultures were used for ELISA assays to measure pro-inflammatory and anti-inflammatory cytokines. WT microglia showed robust TNF-α secretion following amyloid challenge, confirming activation, whereas *Pml-/-* microglia produced significantly lower TNF-α **(**Fig. 3D**)**. In addition, we examined IL-10 expression and we found that both WT and *Pml-/-* microglia showed increased IL-10 production after oAβ_{1-42} treatment, whereas *Pml-/-* microglia displayed significantly lower IL-10 levels than WT cells **(**Fig. 3E**)**. These data indicate that *Pml-/-* primary microglia show impaired activation, viability and cytokine responsiveness following a β-amyloid challenge. Attenuated induction of TREM2 and imbalance between pro- and anti-inflammatory cytokines suggest an impairment in microglial immune competence, in line with *in vivo* findings in the hippocampus **(**Fig. 2B, C**).**

A key physiological function of microglia *in vivo* is the clearance by phagocytosis of apoptotic cells, cellular debris and pathogenic aggregates like amyloid peptides [15]. To determine whether PML influences this function, we examined the phagocytic capacity of WT and *Pml-/-* microglia using fluorescent latex beads. Cells were incubated with microspheres for 1.5, 3 and 6 hours and bead uptake was assessed by confocal microscopy. *Pml-/-* microglia exhibited reduced phagocytic activity at 3h and 6h, compared to WT cells **(**Fig. 3F, G**)**, supporting a role of PML in the phagocytic-clearance capacity of microglia. Collectively, these data suggest that PML is critical for maintaining microglial homeostasis and reactivity under amyloid stress, with its deficiency potentially worsening amyloid pathology and neuroinflammation.

3.3. PML loss exacerbates amyloid deposition in 5xFAD mice

To investigate how PML influences Aβ pathology and Alzheimer's disease related phenotypes, we crossed *Pml-/-* mice and 5xFAD mice to generate 5xFAD *Pml-/-* mice, which were born at the expected Mendelian frequency and presented no developmental defects. RT-qPCR analysis confirmed *Pml* expression in WT and 5xFAD mice and its absence in *Pml-/-* and 5xFAD *Pml-/-* littermates **(Fig. S4A)**. At 6 months of age, high content microscopy analysis revealed that 5xFAD *Pml-/-* mice exhibited significantly augmented amyloid burden characterized by increased amyloid plaque area in the hippocampus and restrosplenial cortex (RSC), compared to 5xFAD controls **(**Fig. 4A, B **and Fig. S4B, C)**, indicating that loss of PML exacerbates Aβ deposition in the 5xFAD background. Interestingly, we found a higher Aβ plaque deposition in females that was even more pronounced in the 5xFAD *Pml-/-* mice **(**Fig. 4B, **Fig. S4C)**, suggesting sex-specific effects of PML function.

Soluble Aβ oligomers are highly neurotoxic and tend to aggregate into fibrils and finally compact plaques [44]. To determine whether PML influences soluble and insoluble forms of Aβ, we quantified $A\beta_{1-42}$ in the soluble (phosphate buffered saline (PBS)-extracted) and insoluble (guanidine -extracted) brain fractions using ELISA. Consistent with the increased amyloid burden observed in 5xFAD *Pml-/-* mice, we detected increased ratio of $A\beta_{42/40}$ in both brain fractions **(**Fig. 4C**)**, which is strongly associated with early onset and faster progression of pathology, aggravating neurodegeneration [45]. These data suggest that PML acts to limit Aβ aggregation in 5xFAD mice.

3.4. 5xFAD *Pml-/-* mice exhibit altered glial dynamics in the hippocampus

Given that PML expression is enriched in reactive microglia in the 5xFAD hippocampus **(**Fig. 1A**)** and that *Pml-/-* microglia exhibit weak activation and phagocytosis both *in vivo* **(**Fig. 2B, C, E, F**)** and *in vitro* **(**Fig. 3**)**, we investigated how PML loss affects microglial activation in Aβ-driven pathology. Immunohistochemistry analysis in 6-month old 5xFAD *Pml-/-* mice revealed reduced IBA1-positive microglia density in the hippocampus and the RSC **(**Fig. 4D **and Fig. S4D)** and decreased TREM2 expression compared to 5xFAD controls **(**Fig. 4E, F **and Fig. S4E, F)**. In addition, we assessed microglial morphology in the hippocampus by performing skeletal and Sholl analyses[46] on IBA1-stained sections. 5xFAD *Pml-/-* microglia displayed a reduction in the number of branches, junctions, triple and quadruple junctions, compared to 5xFAD controls **(Fig. S4G)**. Sholl analysis further confirmed a significant decrease in the number of intersections in 5xFAD *Pml-/-* microglia **(Fig. S4H)**. These changes in microglial morphology indicate diminished branching complexity and a transition toward a less reactive or dystrophic state, consistent with the overall attenuation of microglial reactivity observed in PML-deficient 5xFAD mice. Moreover, PML-deficient 5xFAD mice showed increased death of MAP2 + neurons in DG and RSC and to a lesser extent in CA1 and CA3 regions as shown by elevated cleaved caspase-3 expression **(**Fig. 4G, H **and Fig. S4I, J)**. Our findings indicate that PML deficiency impairs microglial activation and recruitment to Aβ plaques and accelerates Aβ deposition, thereby contributing to neuronal degeneration.

Astrocytes, as key regulators of brain architecture and homeostasis, play crucial roles in the progression of neurological diseases. In models of AD, reactive astrocytes are associated with neuroinflammation, brain damage and cognitive decline [47, 48]. In a previous study, we demonstrated that *Pml-/-* hippocampi exhibit significantly increased presence of astrocytes and enhanced activation of the transcription factor STAT3, compared to WT controls [37]. To further investigate how PML loss influences astrocytic responses during amyloid pathology, we performed immunohistochemistry analyses in 6-month-old 5xFAD and 5xFAD *Pml-/-* mice. We detected pronounced reactive astrogliosis, particularly in areas close to amyloid plaque deposits, with 5xFAD *Pml-/-* mice exhibiting a higher density of GFAP-positive astrocytes in the hippocampal areas CA1, CA3, and the RSC compared to 5xFAD controls **(**Fig. 5A, B, **Fig. S5A, B)**. In the DG, astrocyte reactivity was elevated but showed comparable density between 5xFAD genotypes **(**Fig. 5A, B**)**. As shown in Fig. 5C hypertrophic $GFAP^+$ astrocytes cluster around amyloid plaques in both 5xFAD and 5xFAD *Pml-/-* mice. However, in the absence of PML,

astrocytes were positioned in closer proximity to plaques, extending their processes toward amyloid deposits, likely forming a physical barrier against microglial access and phagocytosis. Consistent with these observations, protein analysis of whole-brain lysates indicated increased levels of activated STAT3 in 5xFAD *Pml-/-* mice **(**Fig. 5D, **Fig. S5C)**, a proinflammatory cytokine inducer connected to Aβ production[49] and a hallmark of astrogliosis [50]. Together, these findings suggest that PML loss enhances astrocyte reactivity (reactive astrogliosis) and STAT3 activation during amyloid pathology, potentially creating an astroglial barrier that interferes with microglial access to Aβ plaques.

3.5. PML loss reprograms the hippocampal transcriptome in a sex-dependent manner

To further delineate the effects of PML deficiency on amyloid pathology at the molecular level, we performed RNAseq analysis of hippocampi, isolated from 6-month old WT, *Pml-/-*, 5xFAD and 5xFAD *Pml-/-* mice. We compared the transcriptomes of *Pml-/-*, 5xFAD, 5xFAD *Pml-/-* with their relative controls, as shown in **Fig. S6A.** Given that Alzheimer's disease exhibits pronounced sex differences in progression and transcriptional signatures [51], we also analyzed male and female samples separately. We performed functional analysis for deregulated gene ontology (GO) pathways, employing the over-representation analysis (ORA). Initially, we compared the transcriptome of *Pml-/-* hippocampi to the WT (**Fig. S6B-E**) and detected downregulation of pathways associated with synapse organization in both sexes and circadian rhythm in males. In the upregulated categories, we found axonogenesis, regulation of neurogenesis and synapse organization indicating that ablation of PML may induce re-wiring of the neuronal system **(Fig. S6C, E)**. Moreover, in males, PML loss caused the upregulation of functions related to cell death in response to stresses **(Fig. S6E)** [52]. These findings suggest a sex-specific bias in the absence of PML.

Pathway analysis in 5xFAD compared to WT animals **(Fig. S6F-I)**, showed downregulation of pathways associated with mitochondria functions in females **(Fig. S6G)** while axonogenesis, dendrite development, learning and memory in males **(Fig. S6I)**. Upregulated pathways related to activation of immune response, microglial activation, cell migration, gliosis, T cell activation and MHC-II antigen processing and presentation **(Fig. S6G, I)**, in agreement with previous studies [53].

In 5xFAD *Pml-/-* females compared with 5xFAD controls, we identified 233 differential expressed genes (DEGs), consisting of 171 downregulated and 62 upregulated genes (padj < 0.05) **(**Fig. 6A **and Table S4)** whereas males displayed 64 DEGs **(**Fig. 6C**)**, consisting of 5 downregulated and 59 upregulated genes (padj < 0.05) **(Table S4)**. Functional analyses for enriched pathways in females, revealed the suppression of ameboidal cell migration pathway that is important for microglia in AD, including *Actn4*, *Akt3*, *Dock1* and *Edn3* [54]. In addition, axonogenesis, dendrite development and synapse organization pathways including *Clasp2*, *Foxp1*, *Adam10*, *Ncam1* and *Picalm*, were suppressed **(**Fig. 6B**)**. The same analysis for the males showed the downregulation of peroxisomal functions **(**Fig. 6D**)** including *Acot5*, *Amacr* and *Ide* that encode for proteins that regulate fatty acid and glucose homeostasis and are emerging AD pathology modulators [55]. Furthermore, pathways related to metabolic processes, cell movement, DNA

repair and immunoglobulin mediated immune-response were also downregulated **(Fig. S6J)**. In females, upregulated pathways included protein degradation and response to starvation, probably reflecting imminent need for aggregate clearance **(**Fig. 6B**)**. In males, chromatin remodeling, NOTCH signaling and EMT transition, were upregulated **(**Fig. 6D**)**. We directly compared deregulated genes between females and males, in 5xFAD *Pml-/-* vs 5xFAD **(**Fig. 6E**)**. In addition to identifying uniquely deregulated genes of either mouse genetic background in males (blue) and females (red), we also detected a class of commonly deregulated genes (Violet) that are downregulated in females and upregulated in males **(Table S5)**, pointing to PML-dependent sex differences. These 50 genes are functionally related with the organization of synapses, axon guidance, mRNA processing, ERK and NOTCH pathways (**Fig. S6K**). We have found that the human homologues of these genes in scRNA-seq datasets from control and AD patients [56], are mainly expressed in excitatory and to lesser extend in inhibitory neurons **(Fig. S6L)**. Moreover the majority of these genes are highly expressed in low amyloid burden human samples **(Fig. S6M)**.

Given that PML is important for regulating functions in microglia, the brain's resident immune cells, we proceeded to investigate changes in immune response related genes. Several genes associated with activation of immune responses, including antigen presentation, were downregulated in 5xFAD *Pml-/-* mice in both females and males **(**Fig. 6F**)**. Moreover, we examined genes upregulated in disease associated microglia (DAM) relative to homeostatic microglia [21]. As depicted in Fig. 6G, the activation of many DAM genes was restrained in 5xFAD *Pml-/-* mice, suggesting compromised microglial activation. Microglial cell activation, by either infection, trauma, or protein aggregates like amyloid-β, results in the production of reactive oxygen species (ROS) and reactive nitrogen species (RNS) as part of their defense mechanisms. As shown in **Fig. S6N** we detected reduced expression of genes related with antioxidant activity. Importantly, both female and male 5xFAD *Pml-/-* mice demonstrated decreased expression of genes regulating synaptic plasticity **(Fig. S6O)**, in accordance with increased neuronal death **(**Fig. 4G, H**)**. Collectively, these findings suggest that PML deficiency alters the hippocampal transcriptome in a sex-dependent manner and compromises the immune and synaptic gene expression patterns, among others.

3.6. PML promotes microglial immune competence and efficient amyloid plaque clearance

Given that the functional and gene expression findings highlighted microglia as major PML target cells **(**Fig. 2–3, 6G**)**, we hypothesized that the increased amyloid burden in 5xFAD *Pml-/-* mice might result from defective ability of microglial to mobilize an efficient DAM or a more general immune response **(**Fig. 6F, G**)**. To test this hypothesis, we isolated and immunophenotyped primary microglia from 6-month old WT, *Pml-/-*, 5xFAD and 5xFAD *Pml-/-* mice. Flow cytometry analysis of $CD11b^{+}$ $CD45^{int}$ microglial populations revealed increased expression of MHC-II and CD86 surface markers, members of the disease-associated microglia (DAM) phenotype that are both connected to antigen presentation and activation of T lymphocytes, in 5xFAD mice, as expected **(**Fig. 7A-C **and Fig. S7A)**. In contrast, 5xFAD *Pml-/-* microglia showed markedly reduced levels of both markers, despite exacerbated amyloid

deposition and neurotoxicity compared with 5xFAD controls (Fig. 7A-C). Microglial cells from WT and *Pml-/-* brains showed no significant expression of MHC-II and CD86. Furthermore, RT-qPCR analysis of FACs-sorted microglia from 5xFAD and 5xFAD *Pml-/-* brains, confirmed decreased gene expression of anti-inflammatory cytokines in the absence of *Pml* (Fig. 7D), supporting the transcriptomics data, indicating that *Pml-/-* microglial cells are defective in both innate and adaptive immune responses.

The degree of lysosomal acidification and the activity of its enzymes are critical for breaking down endogenous cellular waste as well as ingested proteins, such as amyloid deposits [20–22]. Consequently, lysosomal efficiency directly influences microglial function and shapes their activation state during neuroinflammation. Microglia depend on proper lysosomal acidification and functions to facilitate the cellular degradation and recycling system [57–59] for both phagocytosis and antigen peptide processing. Lysosomal acidification and its enzyme activities are critical for degradation of endogenous cellular waste as well as ingested proteins, such as amyloid peptides [59–61], thus influencing microglial function and determining their activation in neuroinflammation. Therefore, we tested whether lysosomal activity correlates with impaired microglia phagocytosis in 5xFAD *Pml-/-* mice. To analyze lysosomal acidification, we performed flow cytometry experiments in primary microglia from 6-month old mice (WT, *Pml-/-*, 5xFAD, 5xFAD *Pml-/-*), employing lysosensor-DND189, a dye that is sensitive to pH alteration in lysosomes. Lysosensor assays revealed increased lysosomal acidification in 5xFAD microglia, in line with increased MHC-II expression and microglia activation, whereas 5xFAD *Pml-/-* microglia exhibited a significant reduction in lysosomal activity (Fig. 7E, F). To evaluate the role of the above in amyloid clearance by microglia, we examined the co-localization of β-amyloid and lysosomes, visualized by Thioflavin-S and anti-CD68 phagolysosomal staining respectively, in hippocampal sections of 5xFAD and 5xFAD *Pml -/- mice.* 5xFAD *Pml*-depleted microglia showed a significant reduction in the volume of ThioS + plaques internalized within CD68 + phagosomes compared to WTs (Fig. 7G, H). Also, plaque-associated CD68 staining was lower in 5xFAD *Pml-/-* mice, indicating reduced microglial Aβ engulfment (Fig. 7G). Together, these findings demonstrate that PML deficiency disrupted key microglial immune and protein degradation pathways, leading to reduced antigen presentation, impaired lysosomal acidification and defective Aβ clearance. This dysfunction likely underlies the exacerbated amyloid burden and neurodegeneration observed in 5xFAD *Pml-/-* mice.

3.7. PML ablation exacerbates the cognitive deficits of 5xFAD mice

5xFAD mice typically develop memory impairments around 4–5 months of age when amyloid plaques and neuroinflammation are present [41]. To evaluate the impact of *Pml* loss-of-function on cognitive performance, we conducted the object location task (OL) which is a hippocampus-dependent spatial object memory test, in 6-month-old male and female mice (Fig. 8A). Control mice normally spend more time exploring the relocated object, indicating intact spatial memory [40]. WT mice spent more time exploring the newly located object, compared to other genotypes (Fig. 8B, **and Fig. S8A-C)**. Object location memory was impaired across sexes in *Pml-/-* and both 5xFAD genotypes (5xFAD and 5xFAD *Pml-/-*), indicating deficits in spatial recognition performance (Fig. 8C). Importantly, *Pml-/-* showed a

reduced discrimination index compared to WT controls. Both 5xFAD and 5xFAD *Pml-/-* mice performed worse than WT animals (Fig. 8C), in line with previous reports of OL memory disruption in AD models [40, 62, 63].

Aβ pathology is known to reduce exploratory behavior and induce anxiety-like and hyperactive phenotypes in transgenic models of AD [64]. To examine the effect of PML deficiency on these behaviors, we performed the open field test (OFT) in WT, *Pml-/-*, 5xFAD and 5xFAD *Pml-/-* mice (Fig. 8D). During the 10 min free exploration period, *Pml-/-* mice exhibited increased time spent in the center zone (Fig. 8E), increased distance in the center zone (Fig. 8F) and increased number of entries to the center zone (Fig. 8G), relative to WT controls reflecting decreased anxiety and thigmotaxis, in agreement with previous studies [65]. Similarly, 5xFAD *Pml-/-* mice exhibited increased distance in the center zone (Fig. 8F) and higher number of entries to the center zone (Fig. 8G) relative to WT controls, albeit the time spent in the center zone was not significantly different from WT (Fig. 8E). On the contrary, the number of entries in the center zone was substantially lower in the 5xFAD compared to *Pml-/-* and 5xFAD *Pml-/-* groups. Importantly, the total distance traveled and average speed were similar among all groups suggesting that they all bear intact locomotor activity (Fig. 8H, I). These findings suggest that 5xFAD *Pml-/-* exhibit a similar phenotype of reduced anxiety and impulsivity as the *Pml-/-* animals. This interpretation is corroborated by the number of animals exhibiting stereotypical jumping behavior [66], shown in **(Fig. S8D and Movie S1**). Both *Pml-/-* and 5xFAD *Pml-/-* groups have a much larger percentage of animals that exhibit such jumping behaviors compared to WT and 5xFAD groups. Together, these findings suggest that PML depletion increases the impulsivity phenotype in the context of Aβ pathology in the 5xFAD background and contributes to hippocampus-dependent behavioral deficits, suggesting an important role for PML in preserving cognitive function during amyloid pathology

4. Discussion

Alzheimer's disease is characterized by the buildup of toxic amyloid-β (Aβ) and TAU protein, which trigger chronic neuroinflammation and progressive neuronal loss, ultimately leading to learning and memory impairments in patients. Understanding the molecular, cellular and physiological pathways underlying each stage of disease progression is therefore essential for developing effective therapeutic strategies. Previous work from our lab, has shown that embryonic neural stem cells (eNSC) isolated from *Pml-/-* mice are more vulnerable to amyloid-β toxicity than control cells and display proteostatic and mitochondrial defects reminiscent of neurodegeneration [37]. In this study, we examined the involvement of PML in amyloid pathology using both an acute model of neuroinflammation and the 5xFAD mouse model.

The functions of PML in inflammation are well characterized and highly context and cell-type dependent [31]. Although PML has been shown to exert either anti- or pro-inflammatory effects through both nuclear and cytoplasmic mechanisms [67], its role in amyloid-induced neuroinflammation is unclear. Our data show that PML is transcriptionally upregulated by intracerebroventricular o$A\beta_{1-42}$ administration and that in turn, PML is required for the hippocampal immune response. Furthermore, PML-deficient

primary microglia exhibited reduced survival, activation, and phagocytic capacity. Previously, a protective role for PML in innate immune responses, inflammation, and microglial activation has also been reported in a hypoxic–ischemic encephalopathy model [32]. Notably, during neuroinflammation, PML protected against cell death and apoptosis, an effect consistent with cellular context dependent roles in various systems, including cancer, that contrasts with its well-known pro-apoptotic, tumor-suppressive functions [31, 68–70].

In Neurodegenerative diseases (NDD), the accumulation of misfolded proteins constitutes an early molecular event that triggers neuroinflammation and leads to neuronal death. A role for PML in “dissolving” toxic aggregates has been reported for mutant Poly Q containing ataxin protein [30, 34], and TDP-43 [71, 72]. In eNSC, we discovered that PML potentiates the autophagic and proteasomal pathways of protein degradation, thus restraining the accumulation of aggregates [37]. Although nuclear aggregates of APP-CT50 fragments together with PML and FE65 have been detected in aged human brains [73], the contribution of PML to AD pathology has not been determined.

To address this gap, we first determined that PML expression declines faster in 5xFAD mice (by 2 months old) at levels comparable to 6 and 12 months old WT mice. These results align with prior evidence describing age-related decreases in PML expression [35]. We next examined the 5xFAD amyloid pathology progression in a PML WT or knock out background.

We show here that PML behaved as a protective factor against AD; in its absence, 5xFAD mice exhibited exacerbated amyloid-β plaque, with a more pronounced effect in females relative to males. Moreover, in the absence of PML the Aβ42/40 ratio was increased, pointing to the acceleration of pathology progression, and accompanied by enhanced neuronal death. Furthermore, the activation state of microglia was reduced as manifested by the diminished expression of the specific markers IBA1 and TREM2 and decreased branching complexity, which correlate with reduced detection and engulfment of amyloid-β species [74, 75]. In contrast to microglia, astrocytes exhibited increased reactivity, in line with elevated STAT3 activation. An imbalance between microglial and astrocytic responses may further hamper the amyloid plaque clearance. In this context, PML has been shown to inhibit STAT3 activation [76], thereby restraining its neuroinflammatory and AD promoting functions [50, 77].

To characterize the molecular pathways that are (de)regulated by PML loss in WT and 5xFAD genotypes, we performed transcriptomic analysis of hippocampi from WT, *Pml-/-*, 5xFAD and 5xFAD *Pml-/-* mice. PML loss per se resulted in significant expression changes in genes involved in diverse functional categories related to synaptic organization, structure and activity. These gene expression changes were consistent with the cognitive deficiencies of the *Pml-/-* mice that we report here.

PML ablation in the 5xFAD background induced pronounced sex-dependent transcriptional alterations in accordance with the increased amyloid pathology observed in female 5xFAD *Pml-/-* mice. A sex specific role for PML has previously been reported in the context of tumorigenesis mediated by mutant P53 protein in mice [78], although a mechanistic insight is still missing. Comparing 5xFAD *Pml-/-* mice with the 5xFAD, we noticed the suppression of functional categories related to synaptic plasticity and immune

system activation. Furthermore, differential expression analyses between females and males revealed a cluster of 50 genes that were discordantly regulated between the sexes in the 5xFAD *Pml-/-* genotype. Notably the human homologues of these genes correlated with human pathology [56], underscoring their potential relevance to AD.

In agreement with the transcriptomic data, microglia isolated from 5xFAD *Pml-/-* mice exhibited a diminished capacity for antigen presentation processes, including reduced expression of MHC molecules, cytokine production, and lysosomal activity. Together, these findings indicate that PML is essential for maintaining the immunological competence of microglia.

Considering that PML ablation in the 5xFAD background increased amyloid plaque deposition and compromised microglial immune responses and amyloid clearance, we evaluated the cognitive performance of *Pml-/-*, 5xFAD and 5xFAD *Pml-/-* mice, relative to the WT. All three animal groups exhibited deficits in spatial memory, manifested as reduced exploration time of a spatially displaced object in the OL task.

Interestingly, *Pml-/-* mice exhibited deficient spatial recognition and increased impulsivity compared to the WT animals although they displayed reduced anxiety, consistent with a previous report [65]. Loss of PML in the 5xFAD mice resulted in similar defects, lowering anxiety and enhancing the impulsivity traits of the 5xFAD mice, as measured by the Open-Field test, thus impacting related behaviors.

In summary, loss of PML resulted in an exacerbation of multiple aspects of AD pathophysiology, including amyloid accumulation, microglial deficiency, impairment of anti-inflammatory mechanisms, neurotoxicity along with cognitive dysfunctions. Microglia represent the principal immune cells of the central nervous system, exhibiting common transcriptional and phenotypic shifts during neurodegeneration and aging [79, 80]. We propose that PML, through its functions in microglia, is both an effector and a marker of aging/neurodegeneration and that its loss may therefore accelerate neuronal pathology and disease progression. Thus, restoring or enhancing PML activity, or selectively targeting its downstream effectors, may represent a promising strategy to modulate neuroinflammation, improve amyloid clearance, and preserve neuronal function in Alzheimer's disease.

Abbreviations

AD
Alzheimer's disease
TAU
Tubulin associated unit
Aβ
Amyloid beta
APP
Amyloid precursor protein
GWAS

Genome-wide association studies
TREM2
Triggering Receptor Expresses on Myeloid Cells 2
CD33
Myeloid cell surface antigen CD33
INPP5D
Inositol Polyphosphate-5-Phosphatase D
PLCG2
Phospholipase C Gamma 2
BIN1
Bridging integrator 1
PICALM
Phosphatidylinositol Binding Clathrin Assembly Protein
CNS
Central nervous system
DAM
Disease-associated microglia
TYROBP
TYRO protein tyrosine kinase-binding protein
APOE
Apolipoprotein E
PML
Promyelocytic Leukemia Protein
PML-NB
Promyelocytic Leukemia nuclear body
STAT1
Signal transducer and activator of transcription 1
STAT6
Signal transducer and activator of transcription 6
ISG
Interferon stimulated gene
ALS
Amyotrophic lateral sclerosis
FTD
Frontotemporal Dementia
PGC1a
peroxisome proliferator-activated receptor gamma coactivator 1-alpha
PPARγ
Peroxisome proliferator-activated receptor gamma
5xFAD

Five familial Alzheimer's Disease mutations
NSC
Neural stem cells
IBA-1
Ionized calcium-binding adapter molecule 1
WT
Wild type
CA1
Cornu Ammonis 1
CA3
Cornu Ammonis 3
DG
Dentate Gyrus
RSC
Retrosplenial cortex
MAP2
Microtubule-Associated Protein 2
RT-qPCR
Reverse transcription-quantitative polymerase chain reaction
Nos2
Nitric oxide synthase
Cst7
Cystatin F
Spp1
Secreted phosphoprotein 1
Siglec-3
Sialic acid-binding Ig-like lectin 3
FBS
Fetal bovine serum
ELISA
Enzyme-linked immunosorbent assay
TNFα
Tumor necrosis factor α
IL-10
Interleukin-10
STAT3
Signal transducer and activator of transcription 3
RNA-seq
RNA sequencing
GO

Gene ontology
ORA
Overrepresentation analysis
MHC-II
Major histocompatibility complex, class II
DEG
Differentially expressed genes
Actn4
Alpha-actinin-4
Akt3
AKT serine/threonine kinase 3
Dock1
Dedicator of cytokinesis 1
Edn3
Endothelin 3
Clasp2
Cytoplasmic linker associated protein 2
Foxp1
Forkhead box P1
Adam10
ADAM metallopeptidase domain 10
Ncam1
Neural cell adhesion molecule 1
Acot5
Acyl-CoA thioesterase 5
Amacr
Alpha-Methylacyl-CoA Racemase
Ide
Insulin-degrading enzyme
EMT
Epithelial–mesenchymal transition
ERK
Extracellular signal-regulated kinase
ROS
Reactive oxygen species
RNS
Reactive nitrogen species
CD11b
Integrin alpha M (ITGAM)
CD45

Cluster of differentiation 45
CD86
Cluster of differentiation 86
CD68
Cluster of differentiation 68
OL
Object location
OFT
Open field test
NDD
Neurodegenerative disease
TDP-43
TAR DNA-binding protein 43
FE65
Amyloid beta (A4) precursor protein-binding, family B, member 1
P53
Tumor protein p53
PDL
Poly-D-lysine
FBS
Fetal bovine serum
DMEM
Dulbecco's Modified Eagle Medium
ICV
Intracerebroventricular
RT
Room temperature
PBS
Phosphate-buffered saline
PFA
Paraformaldehyde
BSA
Bovine serum albumin
DAPI
4',6-Diamidino-2-phenylindole
TO-PRO3
Thiazole Red
GFAP
Glial fibrillary acidic protein
ROI

Region of interest
MFI
Mean fluorescence intensity
EDTA
Ethylenediaminetetraacetic acid
PMSF
Phenylmethylsulfonyl fluoride
SDS
Sodium dodecyl sulfate
TBST
Tris-buffered saline with Tween 20
FACs
Fluorescence-activated cell sorting
FSC-A
Forward scatter area
SSC-A
Side scatter area
DI
Discrimination index
RIN
RNA integrity number
ANOVA
Analysis of variance
IMBB
Institute of Molecular Biology and Biotechnology
FoRTH
Foundation for Research and Technology Hellas

Declarations

Acknowledgements

We thank the IMBB animal facility and especially D. Tsoukatou for expert technical assistance. We acknowledge the IMBB Genomics Facility staff and especially M. Lavigne for the gene expression profiling. We also thank C. Spilianakis for valuable assistance and discussions and A. K. Hatzopoulos and F. Moretto for critical reading the manuscript and helpful suggestions.

Author contributions

S.S. designed and performed experiments, performed data analysis and figure design, and wrote the manuscript. T.M. performed data analysis. S.P. analyzed transcriptomic data and performed functional

analysis. M.P designed, performed and analyzed behavioral experiments. I.P designed behavioral experiments and performed ICV injections. E.D performed data analysis. D.T assisted with transcriptomic data submission to NCBI-GEO. C.N. supervised computational analyses of transcriptomic data. P.P supervised behavioral experiments, assisted with the interpretation of data and provided funding. J.P. designed experiments and contributed to the writing of the manuscript. A.K. designed and supervised the study, wrote the manuscript, and secured funding. All authors contributed to editing the manuscript.

Funding

This work was supported by funding to A.K. from the H.F.R.I call “Basic research Financing (Horizontal support of all Sciences)” under the National Recovery and Resilience Plan “Greece 2.0” funded by the European Union –Next Generation EU (Project Number: 15511), Greece 2.0, National Recovery and Resilience Plan Flagship (program TAEDR-0535850) and intramural funds from the Institute of Molecular Biology and Biotechnology P.P acknowledges funding from the DendroLeap-Stavros Niarchos Foundation (SNF) and the H.F.R.I. under the “Theodoros Papazoglou” program (Project Number 28056) and COFLEX H.F.R.I. call “Basic research Financing (Horizontal support of all Sciences)” under the National Recovery and Resilience Plan “Greece 2.0” (Project Number: 014941).

Availability of data and materials

All data supporting the findings of this study are available in the paper and its supplementary figures. Further information and requests for resources and reagents should be directed to and will be fulfilled by the lead contact, Androniki Kretsovali (kretsova@imbb.forth.gr). This study did not generate new unique reagents. RNA-seq data generated and analyzed in this study are available at GEO under accession numbers GSE313459.

Reviewer access details

The following secure token has been created to allow review of record GSE313459 (RNA-seq) while it remains in private status: arwhsymipjizxqp

Ethics approval and consent to participate

All mice experiments were approved by the FORTH animal ethics committee. Procedures used for the current studies were approved by the General Directorate of Veterinary Services, Region of Crete (license numbers: A. P. 184380, 90851) and were conducted in accordance with the standard guidelines. This work did not involve the use of material from human subjects.

Consent to publication

All authors have read and approved the final manuscript for publication

Competing interests

The authors declare no competing interests

Author details

[1] Institute of Molecular Biology and Biotechnology (IMBB), Foundation for Research and Technology-Hellas (FORTH), 70013 Heraklion, Crete, Greece. [2] Department of Biology, University of Crete, 70013 Heraklion, Greece. [3] Institute for Bio-Innovation, Biomedical Sciences Research Center "Alexander Fleming", 16672 Vari, Greece. [4] School of Medicine, University of Crete, 70013 Heraklion, Greece.

*Correspondence: kretsova@imbb.forth.gr; Tel.: +30-2810-391191

References

1. Winblad B, Amouyel P, Andrieu S, Ballard C, Brayne C, Brodaty H, et al. Defeating Alzheimer's disease and other dementias: A priority for European science and society. Lancet Neurol. Lancet Publishing Group; 2016. pp. 455–532. https://doi.org/10.1016/S1474-4422(16)00062-4.
2. Arendt T, Brückner MK, Morawski M, Jäger C, Gertz HJ. Early neurone loss in Alzheimer's disease: cortical or subcortical? Acta Neuropathol Commun. 2015;3:10. https://doi.org/10.1186/s40478-015-0187-1.
3. De Strooper B, Karran E. The Cellular Phase of Alzheimer's Disease. Cell. Cell Press; 2016. pp. 603–15. https://doi.org/10.1016/j.cell.2015.12.056
4. Hardy J, Selkoe DJ. The Amyloid Hypothesis of Alzheimer's Disease: Progress and Problems on the Road to Therapeutics. Sci AAAs. 2002;297(5580):353–6. https://doi.org/10.1126/science.1072994.
5. Scheuner D, Eckman C, Jensen M, Song X, Citron M, Suzuki N, et al. Secreted amyloid beta-protein similar to that in the senile plaques of Alzheimer's disease is increased in vivo by the presenilin 1 and 2 and APP mutations linked to familial Alzheimer's disease. Nat Med. 1996;2:864–70. https://doi.org/10.1038/nm0896-864.
6. Selkoe DJ, Hardy J. The amyloid hypothesis of Alzheimer's disease at 25 years. EMBO Mol Med Springer Sci Bus Media LLC. 2016;8:595–608. https://doi.org/10.15252/emmm.201606210.
7. Andrews SJ, Renton AE, Fulton-Howard B, Podlesny-Drabiniok A, Marcora E, Goate AM. The complex genetic architecture of Alzheimer's disease: novel insights and future directions. EBioMedicine Elsevier B. 2023. https://doi.org/10.1016/j.ebiom.2023.104511. .V.
8. Karlsson IK, Escott-Price V, Gatz M, Hardy J, Pedersen NL, Shoai M et al. Measuring heritable contributions to Alzheimer's disease: polygenic risk score analysis with twins. Brain Commun. Oxford University Press; 2022;4. https://doi.org/10.1093/braincomms/fcab308
9. Efthymiou AG, Goate AM. Late onset Alzheimer's disease genetics implicates microglial pathways in disease risk. Mol Neurodegener BioMed Cent Ltd. 2017. https://doi.org/10.1186/s13024-017-0184-x.

10. Deczkowska A, Keren-Shaul H, Weiner A, Colonna M, Schwartz M, Amit I. Disease-Associated Microglia: A Universal Immune Sensor of Neurodegeneration. Cell. Cell Press; 2018. pp. 1073–81. https://doi.org/10.1016/j.cell.2018.05.003
11. Butovsky O, Weiner HL. Microglial signatures and their role in health and disease. Nat Rev Neurosci Nat Publishing Group. 2018;622–35. https://doi.org/10.1038/s41583-018-0057-5.
12. Spittau B. Aging microglia-phenotypes, functions and implications for age-related neurodegenerative diseases. Front Aging Neurosci Front Media S A. 2017;9. https://doi.org/10.3389/fnagi.2017.00194.
13. Lemke G. How macrophages deal with death. Nat Rev Immunol Nat Publishing Group. 2019;539–49. https://doi.org/10.1038/s41577-019-0167-y.
14. Bar E, Barak B. Microglia roles in synaptic plasticity and myelination in homeostatic conditions and neurodevelopmental disorders. Glia. John Wiley and Sons Inc.; 2019. pp. 2125–41. https://doi.org/10.1002/glia.23637.
15. De Schepper S, Crowley G, Hong S. Understanding microglial diversity and implications for neuronal function in health and disease. Dev Neurobiol. John Wiley and Sons Inc; 2021. pp. 507–23. https://doi.org/10.1002/dneu.22777.
16. Bernier LP, York EM, Kamyabi A, Choi HB, Weilinger NL, MacVicar BA. Microglial metabolic flexibility supports immune surveillance of the brain parenchyma. Nat Commun Nat Res. 2020;11. https://doi.org/10.1038/s41467-020-15267-z.
17. Roy ER, Wang B, Wan YW, Chiu G, Cole A, Yin Z, et al. Type I interferon response drives neuroinflammation and synapse loss in Alzheimer disease. J Clin Invest Am Soc Clin Invest. 2020;130:1912–30. https://doi.org/10.1172/JCI133737.
18. Rivera-Escalera F, Pinney JJ, Owlett L, Ahmed H, Thakar J, Olschowka JA, et al. IL-1β-driven amyloid plaque clearance is associated with an expansion of transcriptionally reprogrammed microglia. J Neuroinflammation BioMed Cent Ltd. 2019;16. https://doi.org/10.1186/s12974-019-1645-7.
19. Bhaskar K, Maphis N, Xu G, Varvel NH, Kokiko-Cochran ON, Weick JP, et al. Microglial derived tumor necrosis factor-α drives Alzheimer's disease-related neuronal cell cycle events. Neurobiol Dis Acad Press Inc. 2014;62:273–85. https://doi.org/10.1016/j.nbd.2013.10.007.
20. Ennerfelt H, Frost EL, Shapiro DA, Holliday C, Zengeler KE, Voithofer G, et al. SYK coordinates neuroprotective microglial responses in neurodegenerative disease. Cell Elsevier B V. 2022;185:4135–e415222. https://doi.org/10.1016/j.cell.2022.09.030.
21. Keren-Shaul H, Spinrad A, Weiner A, Matcovitch-Natan O, Dvir-Szternfeld R, Ulland TK, et al. A Unique Microglia Type Associated with Restricting Development of Alzheimer's Disease. Cell Cell Press. 2017;169:1276–e129017. https://doi.org/10.1016/j.cell.2017.05.018.
22. Wang S, Sudan R, Peng V, Zhou Y, Du S, Yuede CM, et al. TREM2 drives microglia response to amyloid-β via SYK-dependent and -independent pathways. Cell Elsevier B V. 2022;185:4153–e416919. https://doi.org/10.1016/j.cell.2022.09.033.

23. Krasemann S, Madore C, Cialic R, Baufeld C, Calcagno N, El Fatimy R, et al. The TREM2-APOE Pathway Drives the Transcriptional Phenotype of Dysfunctional Microglia in Neurodegenerative Diseases. Immun Cell Press. 2017;47:566–e5819. https://doi.org/10.1016/j.immuni.2017.08.008.
24. Sala Frigerio C, Wolfs L, Fattorelli N, Thrupp N, Voytyuk I, Schmidt I, et al. The Major Risk Factors for Alzheimer's Disease: Age, Sex, and Genes Modulate the Microglia Response to Aβ Plaques. Cell Rep Elsevier B V. 2019;27:1293–e13066. https://doi.org/10.1016/j.celrep.2019.03.099.
25. Mancuso R, Fattorelli N, Martinez-Muriana A, Davis E, Wolfs L, Van Den Daele J, et al. Xenografted human microglia display diverse transcriptomic states in response to Alzheimer's disease-related amyloid-β pathology. Nat Neurosci Nat Res. 2024;27:886–900. https://doi.org/10.1038/s41593-024-01600-y.
26. Guan D, Kao HY. The function, regulation and therapeutic implications of the tumor suppressor protein, PML. Cell Biosci. BioMed Central Ltd.; 2015. https://doi.org/10.1186/s13578-015-0051-9.
27. Korb E, Finkbeiner S. PML in the brain: From development to degeneration. Front Oncol. 2013. https://doi.org/10.3389/fonc.2013.00242. 3 SEP.
28. Hsu KS, Zhao X, Cheng X, Guan D, Mahabeleshwar GH, Liu Y, et al. Dual regulation of Stat1 and Stat3 by the tumor suppressor protein PML contributes to interferon α-mediated inhibition of angiogenesis. J Biol Chem Am Soc Biochem Mol Biology Inc. 2017;292:10048–60. https://doi.org/10.1074/jbc.M116.771071.
29. Kim YE, Ahn JH. Positive Role of Promyelocytic Leukemia Protein in Type I Interferon Response and Its Regulation by Human Cytomegalovirus. PLoS Pathog Public Libr Sci. 2015;11:1–24. https://doi.org/10.1371/journal.ppat.1004785.
30. Janer A, Martin E, Muriel MP, Latouche M, Fujigasaki H, Ruberg M, et al. PML clastosomes prevent nuclear accumulation of mutant ataxin-7 and other polyglutamine proteins. J Cell Biol. 2006;174:65–76. https://doi.org/10.1083/jcb.200511045.
31. Lunardi A, Gaboli M, Giorgio M, Rivi R, Bygrave A, Antoniou M, et al. A role for PML in innate immunity. Genes Cancer. Volume 2. SAGE Publications Inc.; 2011. pp. 10–9. https://doi.org/10.1177/1947601911402682.
32. Palibrk V, Suganthan R, Scheffler K, Wang W, Bjørås M, Bøe SO. PML regulates neuroprotective innate immunity and neuroblast commitment in a hypoxic-ischemic encephalopathy model. Cell Death Dis Nat Publishing Group. 2016;7. https://doi.org/10.1038/cddis.2016.223.
33. Guo L, Giasson BI, Glavis-Bloom A, Brewer MD, Shorter J, Gitler AD, et al. A cellular system that degrades misfolded proteins and protects against neurodegeneration. Mol Cell Cell Press. 2014;55:15–30. https://doi.org/10.1016/j.molcel.2014.04.030.
34. Chort A, Alves S, Marinello M, Dufresnois B, Dornbierer JG, Tesson C, et al. Interferon beta induces clearance of mutant ataxin 7 and improves locomotion in SCA7 knock-in mice. Brain Oxf Univ Press. 2013;136:1732–45. https://doi.org/10.1093/brain/awt061.
35. Wenger B, Schwegler M, Brunner M, Daniel C, Schmidt M, Fietkau R, et al. PML-nuclear bodies decrease with age and their stress response is impaired in aged individuals. BMC Geriatr BioMed

Cent Ltd. 2014;14:42. https://doi.org/10.1186/1471-2318-14-42.

36. Antoniani F, Cimino M, Mediani L, Vinet J, Verde EM, Secco V, et al. Loss of PML nuclear bodies in familial amyotrophic lateral sclerosis-frontotemporal dementia. Cell Death Discov Springer Nat. 2023;9. https://doi.org/10.1038/s41420-023-01547-2.
37. Spanou S, Makatounakis T, Deligianni E, Papanikolaou S, Samiotaki M, Moretto F, et al. PML is crucial for neural stem cell differentiation, stress tolerance and mitochondrial integrity. Stem Cell Rep Cell Press. 2025;20. https://doi.org/10.1016/j.stemcr.2025.102598.
38. Chock VY, Giffard RG. Development of neonatal murine microglia in vitro: Changes in response to lipopolysaccharide and ischemia-like injury. Pediatr Res Springer Nat. 2005;57:475–80. https://doi.org/10.1203/01.PDR.0000155758.79523.44.
39. Dongre P, Ramesh M, Govindaraju T, Inamdar MS. Asrij/OCIAD1 depletion reduces inflammatory microglial activation and ameliorates Aβ pathology in an Alzheimer's disease mouse model. J Neuroinflammation BioMed Cent Ltd. 2025;22. https://doi.org/10.1186/s12974-025-03415-5.
40. Creighton SD, Mendell AL, Palmer D, Kalisch BE, MacLusky NJ, Prado VF, et al. Dissociable cognitive impairments in two strains of transgenic Alzheimer's disease mice revealed by a battery of object-based tests. Sci Rep Nat Publishing Group. 2019;9. https://doi.org/10.1038/s41598-018-37312-0.
41. Oakley H, Cole SL, Logan S, Maus E, Shao P, Craft J, et al. Intraneuronal β-amyloid aggregates, neurodegeneration, and neuron loss in transgenic mice with five familial Alzheimer's disease mutations: Potential factors in amyloid plaque formation. J Neurosci. 2006;26:10129–40. https://doi.org/10.1523/JNEUROSCI.1202-06.2006.
42. Eskandari-Sedighi G, Crichton M, Zia S, Gomez-Cardona E, Cortez LM, Patel ZH, et al. Alzheimer's disease associated isoforms of human CD33 distinctively modulate microglial cell responses in 5XFAD mice. Mol Neurodegener BioMed Cent Ltd. 2024;19. https://doi.org/10.1186/s13024-024-00734-8.
43. Griciuc A, Patel S, Federico AN, Choi SH, Innes BJ, Oram MK, et al. TREM2 Acts Downstream of CD33 in Modulating Microglial Pathology in Alzheimer's Disease. Neuron Cell Press. 2019;103:820–e8357. https://doi.org/10.1016/j.neuron.2019.06.010.
44. Leng F, Edison P. Neuroinflammation and microglial activation in Alzheimer disease: where do we go from here? Nat Rev Neurol Nat Res. 2021;157–72. https://doi.org/10.1038/s41582-020-00435-y.
45. Pérez-Grijalba V, Romero J, Pesini P, Sarasa L, Monleón I, San-José I, et al. Plasma Aβ42/40 Ratio Detects Early Stages of Alzheimer's Disease and Correlates with CSF and Neuroimaging Biomarkers in the AB255 Study. J Prev Alzheimers Dis Elsevier B V. 2019;6:34–41. https://doi.org/10.14283/jpad.2018.41.
46. Murray CJ, Tunderman ED, Vecchiarelli HA, González Ibáñez F, Tremblay M-È. A comparison of microglial morphological complexity in adult mouse brain samples using 2-dimensional and 3-dimensional image analysis tools. Glial Health Res Elsevier BV. 2025;2:100007. https://doi.org/10.1016/j.ghres.2025.100007.

47. Hall CM, Lasli S, Serwinski B, Djordjevic B, Sheridan GK, Moeendarbary E. Hippocampus of the APPNL–G–F mouse model of Alzheimer's disease exhibits region-specific tissue softening concomitant with elevated astrogliosis. Front Aging Neurosci Front Media SA. 2023;15. https://doi.org/10.3389/fnagi.2023.1212212.
48. Kim JH, Michiko N, Choi IS, Kim Y, Jeong JY, Lee MG, et al. Aberrant activation of hippocampal astrocytes causes neuroinflammation and cognitive decline in mice. PLoS Biol Public Libr Sci. 2024;22. https://doi.org/10.1371/journal.pbio.3002687.
49. Carret-Rebillat AS, Pace C, Gourmaud S, Ravasi L, Montagne-Stora S, Longueville S, et al. Neuroinflammation and Aβ accumulation linked to systemic inflammation are decreased by genetic PKR down-regulation. Sci Rep Nat Publishing Group. 2015;5. https://doi.org/10.1038/srep08489.
50. Reichenbach N, Delekate A, Plescher M, Schmitt F, Krauss S, Blank N, et al. Inhibition of Stat3-mediated astrogliosis ameliorates pathology in an Alzheimer's disease model. EMBO Mol Med Springer Sci Bus Media LLC. 2019;11. https://doi.org/10.15252/emmm.201809665.
51. Sil A, Erfani A, Lamb N, Copland R, Riedel G, Platt B. Sex Differences in Behavior and Molecular Pathology in the 5XFAD Model. J Alzheimer's Disease IOS Press BV. 2022;85:751–74. https://doi.org/10.3233/JAD-210523.
52. Lallemand-Breitenbach V, de Thé H. PML nuclear bodies: from architecture to function. Curr Opin Cell Biol. Elsevier Ltd; 2018. pp. 154–61. https://doi.org/10.1016/j.ceb.2018.03.011
53. Boza-Serrano A, Yang Y, Paulus A, Deierborg T. Innate immune alterations are elicited in microglial cells before plaque deposition in the Alzheimer's disease mouse model 5xFAD. Sci Rep Nat Publishing Group. 2018;8. https://doi.org/10.1038/s41598-018-19699-y.
54. Liu C, Zhang X, Chai H, Xu S, Liu Q, Luo Y, et al. Identification of Immune Cells and Key Genes associated with Alzheimer's Disease. Int J Med Sci Ivyspring Int Publisher. 2022;19:112–25. https://doi.org/10.7150/IJMS.66422.
55. Li H, Wu J, Zhu L, Sha L, Yang S, Wei J, et al. Insulin degrading enzyme contributes to the pathology in a mixed model of Type 2 diabetes and Alzheimer's disease: possible mechanisms of IDE in T2D and AD. Biosci Rep. Portland Press Ltd; 2018. p. 38. https://doi.org/10.1042/BSR20170862.
56. Mathys H, Boix CA, Akay LA, Xia Z, Davila-Velderrain J, Ng AP, et al. Single-cell multiregion dissection of Alzheimer's disease. Nat Nat Res. 2024;632:858–68. https://doi.org/10.1038/s41586-024-07606-7.
57. Iyer H, Shen K, Meireles AM, Talbot WS. A lysosomal regulatory circuit essential for the development and function of microglia. Sci Adv AAAs. 2022;8(35):eabp8321. https://doi.org/10.1126/sciadv.abp8321.
58. Van Acker ZP, Perdok A, Bretou M, Annaert W. The microglial lysosomal system in Alzheimer's disease: Guardian against proteinopathy. Ageing Res Rev. Elsevier Ireland Ltd; 2021. https://doi.org/10.1016/j.arr.2021.101444
59. Plaza-Zabala A, Sierra-Torre V, Sierra A. Autophagy and microglia: Novel partners in neurodegeneration and aging. Int J Mol Sci MDPI AG. 2017. https://doi.org/10.3390/ijms18030598.

60. Mosher KI, Wyss-Coray T. Microglial dysfunction in brain aging and Alzheimer's disease. Biochem Pharmacol. Elsevier Inc.; 2014. pp. 594–604. https://doi.org/10.1016/j.bcp.2014.01.008.
61. Shi F, Yang Y, Kouadir M, Fu Y, Yang L, Zhou X, et al. Inhibition of phagocytosis and lysosomal acidification suppresses neurotoxic prion peptide-induced NALP3 inflammasome activation in BV2 microglia. J Neuroimmunol. 2013;260:121–5. https://doi.org/10.1016/j.jneuroim.2013.04.016.
62. Frye CA, Walf AA. Effects of progesterone administration and APPswe + PSEN1Δe9 mutation for cognitive performance of mid-aged mice. Neurobiol Learn Mem Elsevier B V. 2008;89:17–26. https://doi.org/10.1016/j.nlm.2007.09.008.
63. Bergin DH, Liu P. Agmatine protects against β-amyloid 25-35-induced memory impairments in the rat. Neurosci Elsevier B V. 2010;169:794–811. https://doi.org/10.1016/j.neuroscience.2010.05.004.
64. Ferguson SA, Sarkar S, Schmued LC. Longitudinal behavioral changes in the APP/PS1 transgenic Alzheimer's Disease model. Behav Brain Res Elsevier B V. 2013;242:125–34. https://doi.org/10.1016/j.bbr.2012.12.055.
65. Butler K, Martinez LA, Tejada-Simon MV, Tejada-Simon MV. Impaired Cognitive Function and Reduced Anxiety-Related Behavior in a Promyelocytic Leukemia (PML) Tumor Suppressor Protein-Deficient Mouse. Behav John Wiley Sons Inc. 2013;12(2):189–202. https://doi.org/10.1111/gbb.12014.
66. Lansdell TA, Xu H, Galligan JJ, Dorrance AM, Pérez EA. Effects of Striatal Amyloidosis on the Dopaminergic System and Behavior: A Comparative Study in Male and Female 5XFAD Mice. J Alzheimer's Disease IOS Press BV. 2023;94:1361–75. https://doi.org/10.3233/JAD-220905.
67. Hsu KS, Kao HY. PML: Regulation and multifaceted function beyond tumor suppression. Cell Biosci. BioMed Central Ltd.; 2018. https://doi.org/10.1186/s13578-018-0204-8
68. Lo Y-H, Huang Y-W, Wu Y-H, Tsai C-S, Lin Y-C, Mo S-T et al. Selective inhibition of the NLRP3 inflammasome by targeting to promyelocytic leukemia protein in mouse and human. Blood. ASH Publications; 2013; 18;121(16):3185-94. https://doi.org/10.1182/blood-2012-05-432104
69. Dowling JK, Becker CE, Bourke NM, Corr SC, Connolly DJ, Quinn SR, et al. Promyelocytic leukemia protein interacts with the apoptosis-associated speck-like protein to limit inflammasome activation. J Biol Chem Am Soc Biochem Mol Biology Inc. 2014;289:6429–37. https://doi.org/10.1074/jbc.M113.539692.
70. Missiroli S, Perrone M, Gafà R, Nicoli F, Bonora M, Morciano G, et al. PML at mitochondria-associated membranes governs a trimeric complex with NLRP3 and P2X7R that modulates the tumor immune microenvironment. Cell Death Differ Springer Nat. 2023;30:429–41. https://doi.org/10.1038/s41418-022-01095-9.
71. Wagner K, Keiten-Schmitz J, Adhikari B, Patra U, Husnjak K, McNicoll F, et al. Induced proximity to PML protects TDP-43 from aggregation via SUMO–ubiquitin networks. Nat Chem Biol Nat Res. 2025;21:1408–19. https://doi.org/10.1038/s41589-025-01886-4.
72. Yu X, Zhang H. Come get dissolved in PML bodies. Nat Chem Biol Nat Res. 2025;1306–7. https://doi.org/10.1038/s41589-025-01960-x.

73. Marks D, Heinen N, Bachmann L, Meermeyer S, Werner M, Gallego L, et al. Amyloid precursor protein elevates fusion of promyelocytic leukemia nuclear bodies in human hippocampal areas with high plaque load. Acta Neuropathol Commun BioMed Cent Ltd. 2021;9. https://doi.org/10.1186/s40478-021-01174-x.
74. Davies DS, Ma J, Jegathees T, Goldsbury C. Microglia show altered morphology and reduced arborization in human brain during aging and Alzheimer's disease. Brain Pathol Blackwell Publishing Ltd. 2017;27:795–808. https://doi.org/10.1111/bpa.12456.
75. Fujikawa R, Tsuda M. The Functions and Phenotypes of Microglia in Alzheimer's Disease. Cells MDPI. 2023. https://doi.org/10.3390/cells12081207.
76. Kawasaki A, Matsumura I, Kataoka Y, Takigawa E, Nakajima K, Kanakura Y. Opposing effects of PML and PML/RAR on STAT3 activity. Blood ASH Publications. 2003;101(9):3668–73. 10.1182/blood-2002-08-2474.
77. Hu Y, Zhang X, Zhang J, Xia X, Li H, Qiu C, et al. Activated STAT3 signaling pathway by ligature-induced periodontitis could contribute to neuroinflammation and cognitive impairment in rats. J Neuroinflammation BioMed Cent Ltd. 2021;18. https://doi.org/10.1186/s12974-021-02071-9.
78. Haupt S, Di Agostino S, Mizrahi I, Alsheich-Bartok O, Voorhoeve M, Damalas A, et al. Promyelocytic leukemia protein is required for gain of function by mutant p53. Cancer Res Am Association Cancer Res. 2009;69:4818–26. https://doi.org/10.1158/0008-5472.CAN-08-4010.
79. Sala Frigerio C, Wolfs L, Fattorelli N, Thrupp N, Voytyuk I, Schmidt I, et al. The Major Risk Factors for Alzheimer's Disease: Age, Sex, and Genes Modulate the Microglia Response to Aβ Plaques. Cell Rep Elsevier B V. 2019;27:1293–e13066. https://doi.org/10.1016/j.celrep.2019.03.099.
80. Candlish M, Hefendehl JK. Microglia Phenotypes Converge in Aging and Neurodegenerative Disease. Front Neurol. Front Media S A. 2021. https://doi.org/10.3389/fneur.2021.660720.

Figures

Figure 1

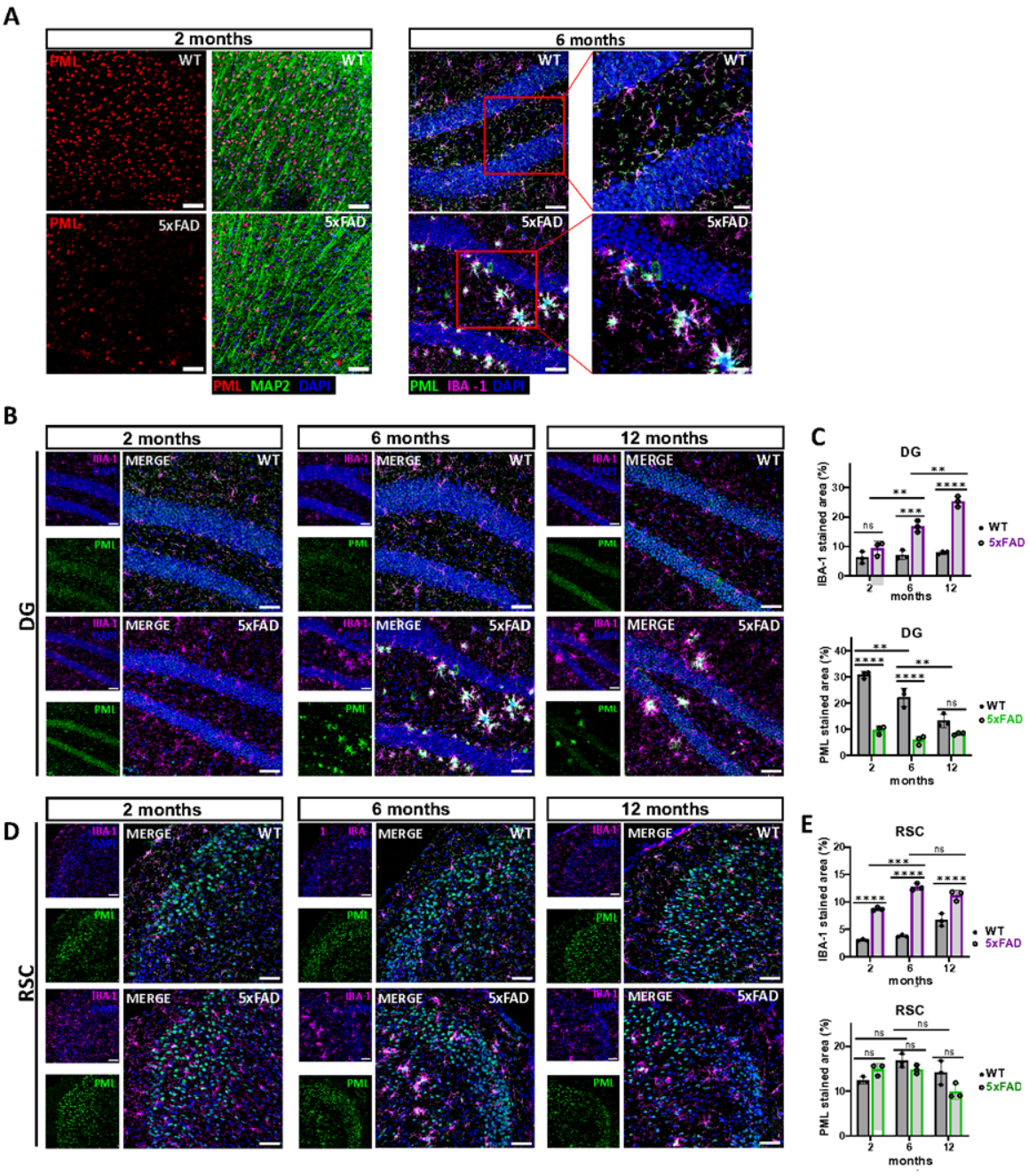


Figure 1

PML expression changes with the progression of amyloid pathology in 5xFAD mice.

(A) Left: Immunofluorescence staining of PML (red), MAP2 (green) in the cortex and hippocampus of 2 months old WT and 5xFAD mice. Right: PML (green) and IBA1 (magenta) in the hippocampus of 6 months old WT and 5xFAD mice. Representative confocal images are shown. Nuclei stained with DAPI.

Scale bar: 50μm. **(B)**Immunofluorescence staining of PML (green) and IBA1 (magenta) in the DG of 2, 6, 12 months old WT and 5xFAD mice. Representative confocal images are shown. Nuclei stained with DAPI. Scale bar: 50μm. **(C)** Quantification of IBA1+ microglia density and percent area covered by PML staining in the DG. 4 sections per mouse (*n*=3 animals per genotype, all males, ** p<0.0041, ***p=0.0003, **** p<0.0001; two-way ANOVA) **(D)** Immunofluorescence staining of PML (green) and IBA1 (magenta) in the RSC of 2, 6, 12 months old WT and 5xFAD mice. Representative confocal images are shown. Nuclei stained with DAPI. Scale bar: 50μm. **(E)**Quantification of IBA1+ microglia density and percent area covered by PML staining in the RSC. 4 sections per mouse (*n*=3 animals per genotype, all males, ***p=0.0001, **** p<0.0001; two-way ANOVA). Graphs show mean values ± S.D.

Figure 2

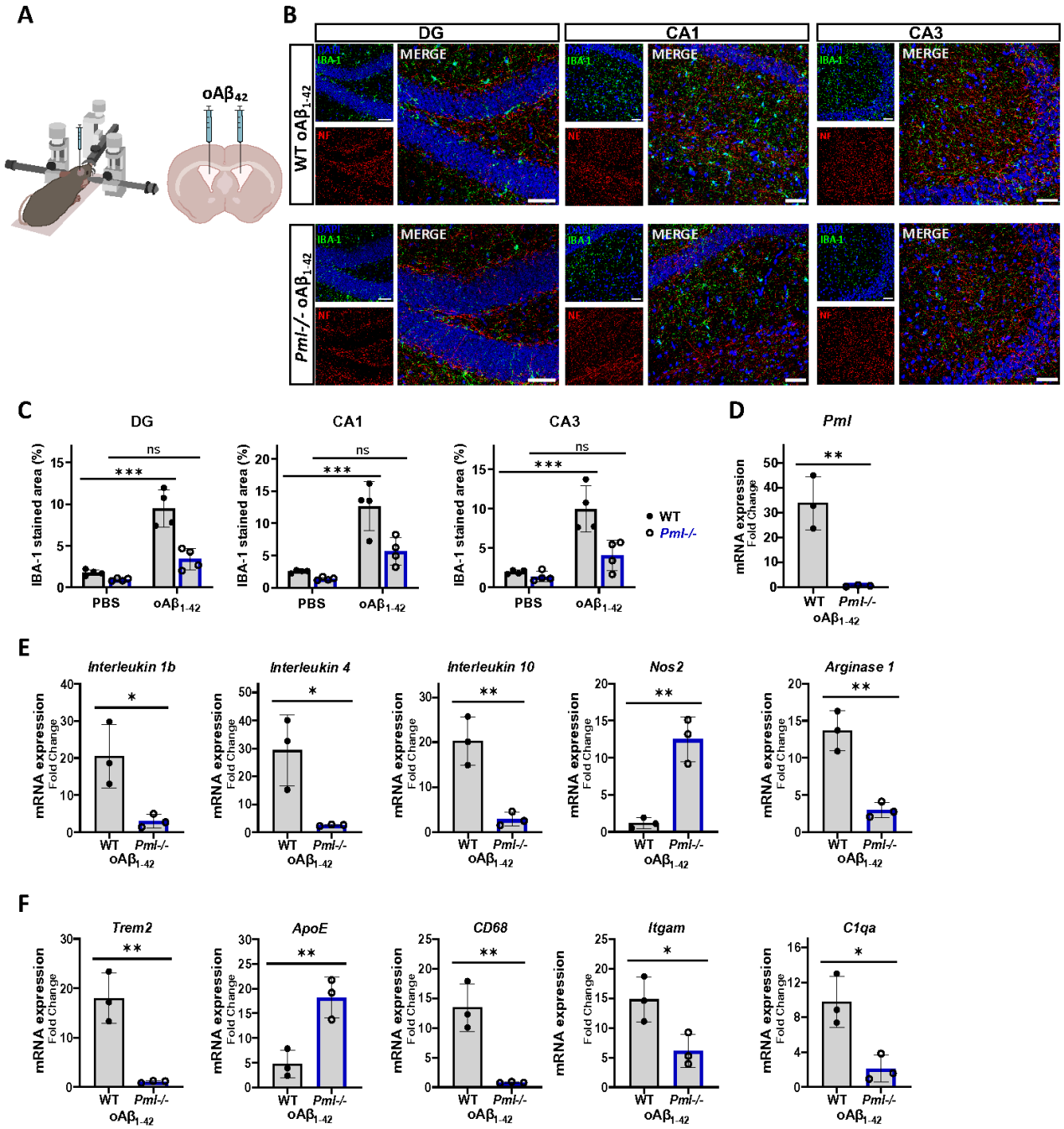


Figure 2

PML is required for innate immune responses to amyloid oligomers in the hippocampus.

(A) Schematic representation of intracerebroventricular injections using a stereotaxic apparatus. **(B)** Immunofluorescence staining of IBA1 (green) and Neurofilament (red) in the DG, CA1 and CA3 of WT and *Pml-/-* mice 72h post injection with Aβ oligomers. Representative confocal images are shown.

Nuclei stained with DAPI. Scale bar: 50μm. **(C)** Quantification of IBA1+ microglia density in the hippocampi of PBS or oAβ_{1-42} injected WT and *Pml-/-* mice. 5 sections per mouse (*n*=4 animals per genotype, all males, ***p<0.0002, **** p<0.0001; two-way ANOVA). **(D)** RT-qPCR analysis for PML expression in the hippocampi of oAβ_{1-42} injected WT and *Pml-/-* mice, normalized to PBS injected. (*n*=3 animals per genotype, all males, **p=0.0058; unpaired t-test). **(E)** RT-qPCR analysis for pro-inflammatory and anti-inflammatory markers in the hippocampi of PBS or oAβ_{1-42} injected WT and *Pml-/-* mice, normalized to PBS injected. (*n*=3 animals per genotype, all males, *p<0.0258, **p<0.0032; unpaired t-test). **(F)** RT-qPCR analysis for disease associated microglia (DAM) genes in the hippocampi of oAβ_{1-42} injected WT and *Pml-/-* mice, normalized to PBS injected. (*n*=3 animals per genotype, all males, *p<0.0332, **p<0.0092; unpaired t-test). Graphs show mean values ± S.D.

Figure 3

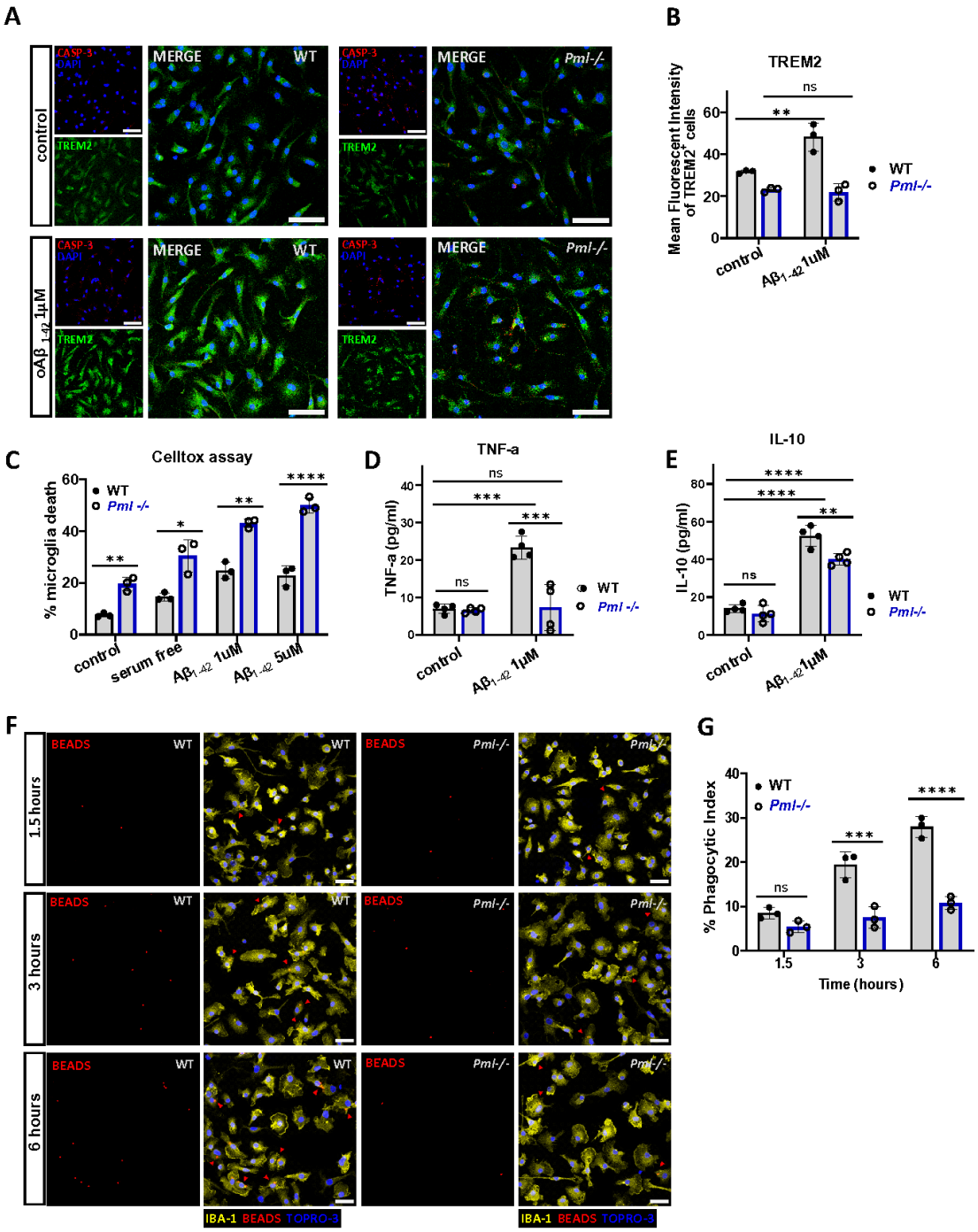


Figure 3

***Pml-/-* microglia exhibit impaired activation, viability and cytokine responsiveness following a β-amyloid challenge.**

(A) Immunofluorescence staining of TREM2 (green) and cleaved CASPASE-3 (red) in primary WT and *Pml-/-*microglia treated with oA$\beta_{1\text{-}42}$ for 48h. Representative confocal images are shown. Nuclei stained

with DAPI. Scale bar: 30µm. **(B)** Quantification of TREM2 in primary microglia cultures, showing mean fluorescent intensity ± S.D (*n*=3 independent replicates, ** p=0.0055; two-way ANOVA). **(C)** CellTox quantification showing percentage of microglia death after treatment with oAβ_{1-42} for 48h (*n*=3 independent replicates, *p=0.0273, **p<0.0051, ****p<0.0001; two-way ANOVA). **(D)** ELISA for TNFa and **(E)** for IL-10 in supernatants of WT and *Pml-/-* primary microglia treated with oAβ_{1-42} for 48h (*n*=4 independent replicates, **p=0.0041, ***p=0.0002, ****p<0.0001; two-way ANOVA). **(F)** Immunofluorescence staining of IBA1 (yellow) and fluorescent microbeads (red) in primary WT and *Pml-/-*microglia. Representative confocal images are shown. Nuclei stained with TO-PRO3. Scale bar: 30µm. **(G)** Quantification of phagocytic index of primary WT and *Pml-/-*microglia (*n*=3 independent replicates, ** p=0.0002, ****p<0.0001; unpaired t-test). Graphs show mean values ± S.D.

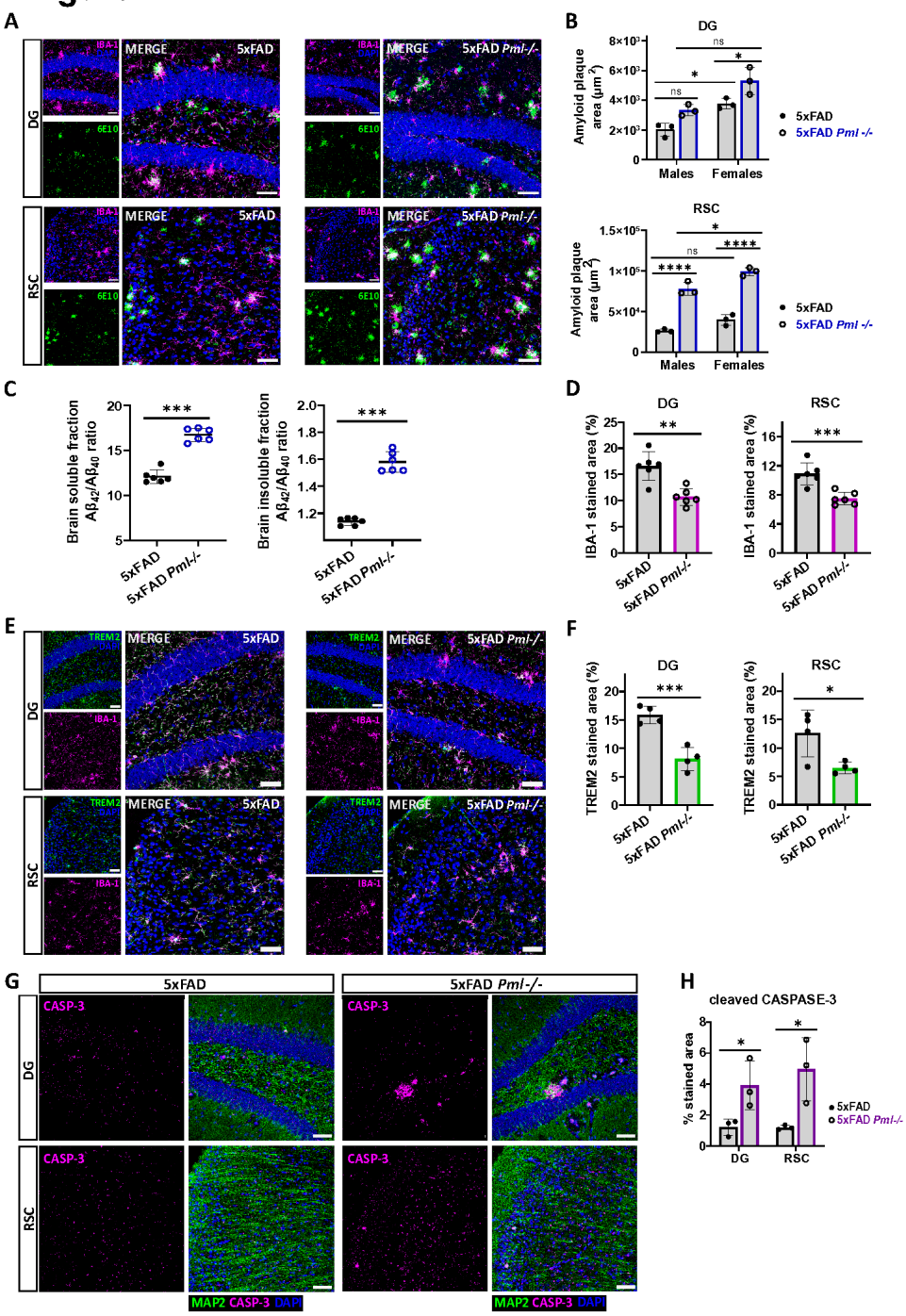


Figure 4

PML depletion impairs microglial recruitment to Aβ plaques and accelerates Aβ deposition in 5xFAD mice.

(A) Immunofluorescence staining of Aβ42 (green) and IBA1 (magenta) in the DG and RSC of 6 month old 5xFAD and 5xFAD *Pml-/-* mice. Representative confocal images are shown. Nuclei stained with DAPI.

Scale bar: 50µm. **(B)** Quantification of amyloid plaque area (µm^2) in the DG and RSC of 6 month old 5xFAD and 5xFAD *Pml-/-* mice. Image analysis performed in Harmony software. (*n*=6 animals per genotype, females and males, *p<0.0447, ***p=0.0003, ****p<0.0001; two-way ANOVA). **(C)** ELISA for Ab42 production in the soluble and insoluble part of the brain in 6 months old 5xFAD and 5xFAD *Pml-/-* mice. (*n*=6 animals per genotype, all males, ***p=0.0005; unpaired t-test). **(D)** Quantification of IBA1+ microglia density in DG and RSC of 6 month old 5xFAD and 5xFAD *Pml-/-* mice. 4 sections per mouse (*n*=6 animals per genotype, all males, **p=0.0011, ***p=0.0008; unpaired t-test). **(E)** Immunofluorescence staining of TREM2 (green) and IBA1 (magenta) in the DG and RSC of 6 month old 5xFAD and 5xFAD *Pml-/-* mice. Representative confocal images are shown. Nuclei stained with DAPI. Scale bar: 50µm. **(F)** Quantification of TREM2+ microglia density in DG and RSC of 6 month old 5xFAD and 5xFAD *Pml-/-* mice. 4 sections per mouse (*n*=4 animals per genotype, all males, *p=0.0279, ***p=0.0009; unpaired t-test). **(G)** Immunofluorescence staining of MAP2 (green) and cleaved-CASPASE-3 (magenta) in the DG and RSC of 6 month old 5xFAD and 5xFAD *Pml-/-* mice. Representative confocal images are shown. Nuclei stained with DAPI. Scale bar: 50µm. **(H)** Quantification of cleaved-CASPASE-3 in DG and RSC of 6 month old 5xFAD and 5xFAD *Pml-/-* mice. 4 sections per mouse (*n*=3 animals per genotype, all males, *p<0.0433; unpaired t-test). Graphs show mean values ± S.D.

Figure 5

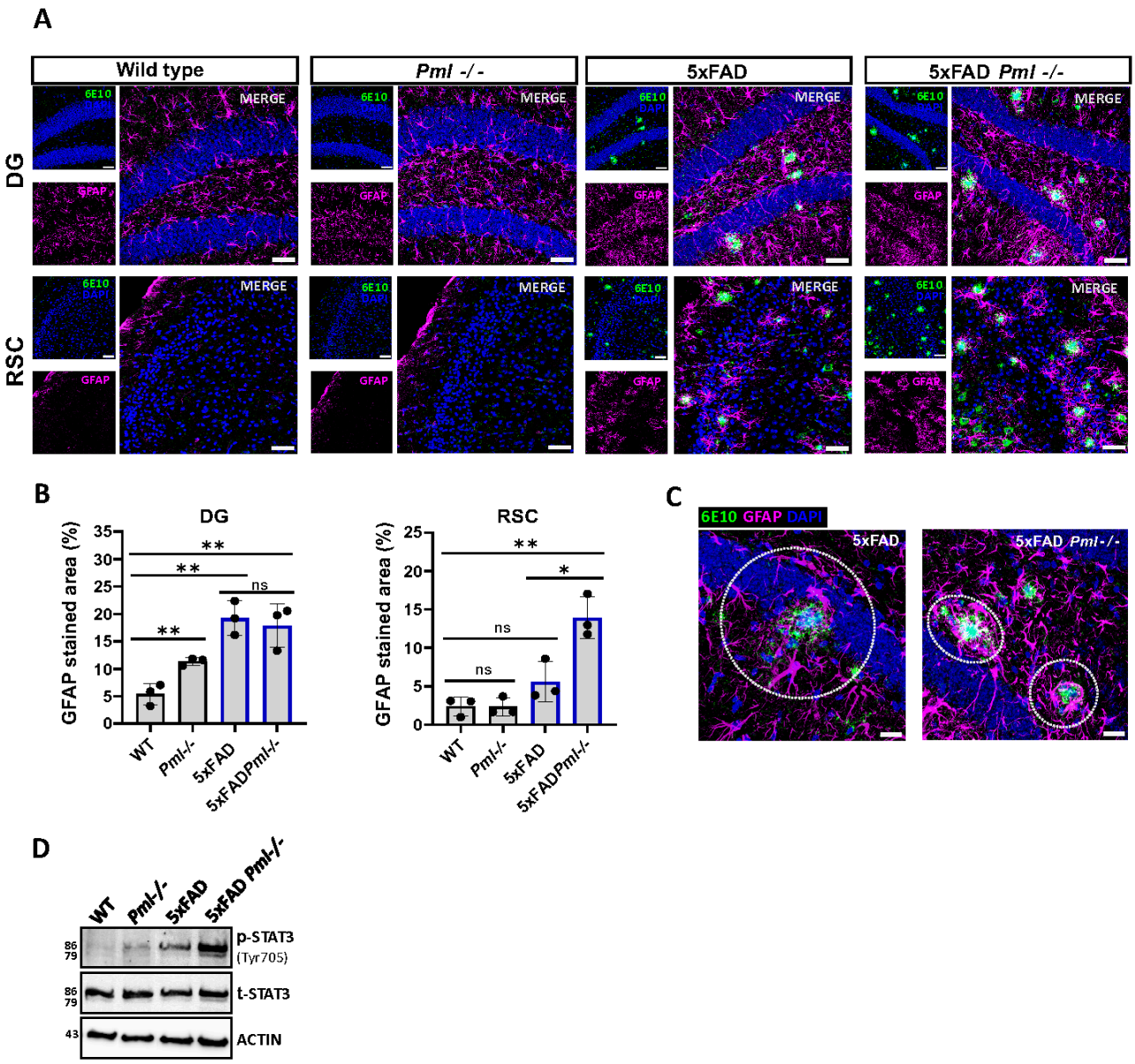


Figure 5

5xFAD *Pml-/-* mice demonstrate pronounced reactive astrogliosis during amyloid pathology.

(A) Immunofluorescence staining of Aβ42 (green) and GFAP (magenta) in the DG and RSC of 6 month old WT, *Pml-/-*, 5xFAD and 5xFAD *Pml-/-*mice. Representative confocal images are shown. Nuclei stained with DAPI. Scale bar: 50µm. **(B)**Quantification of GFAP+ astrocytes in DG and RSC of 6 month mice. 4 sections per mouse (*n*=3 animals per genotype, all males, *p=0.0190, **p<0.0081; unpaired t-test). Graph shows mean values ± S.D. **(C)** Higher magnification of immunofluorescence staining of Aβ42 (green) and

GFAP (magenta) in the DG of 5xFAD and 5xFAD *Pml-/-* 6 month old mice, showing hypertrophic astrocytes and their recruitment in amyloid plaques. Scale bar: 20µm. **(D)**Protein expression analysis of activated STAT3 (Y705) in whole brain lysates of 6 month old mice.

Figure 6

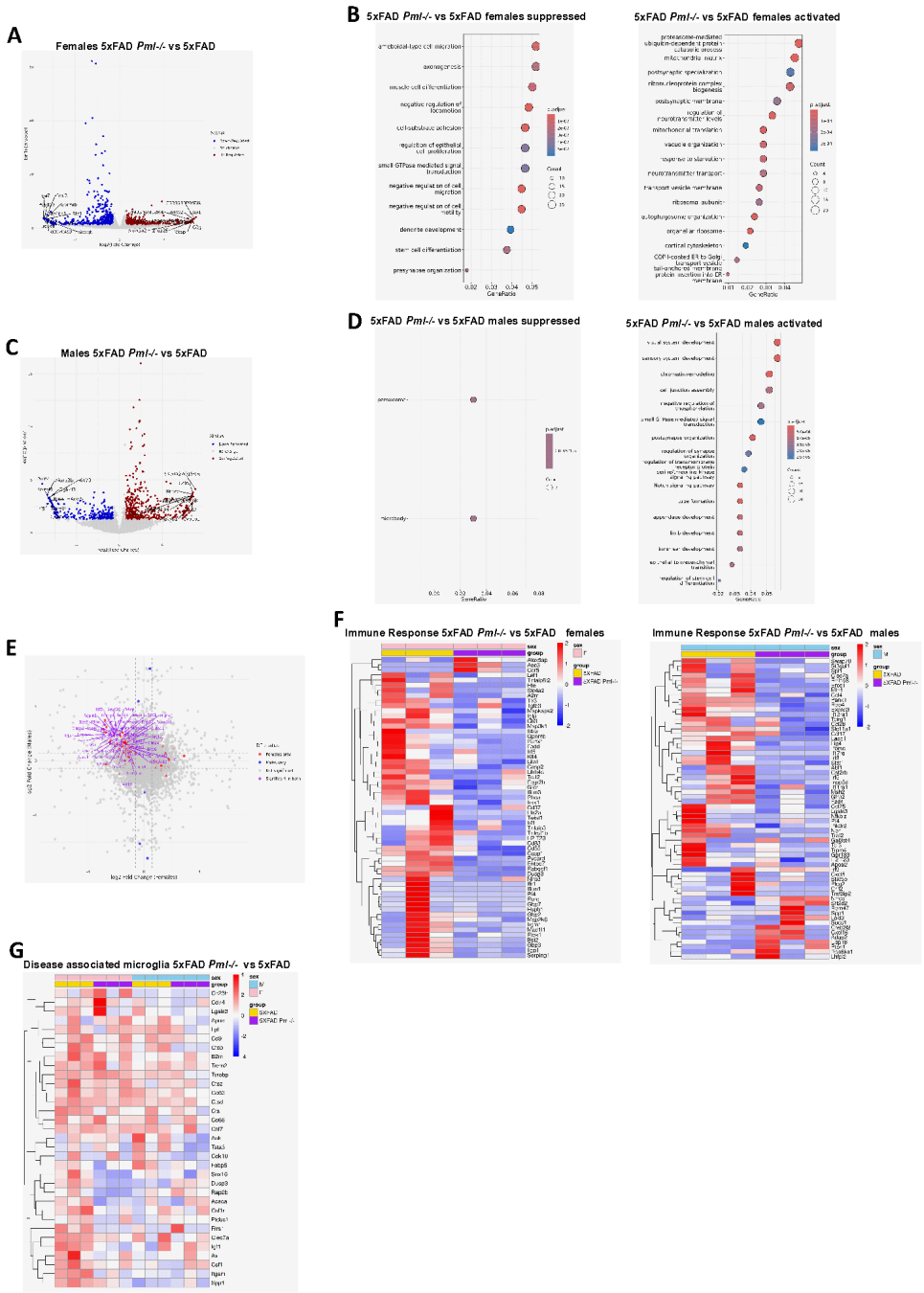


Figure 6

PML deficiency reprograms the hippocampal transcriptome in a sex-dependent manner and compromises immune gene expression.

(A) Volcano plot of differentially expressed genes (DEGs) in hippocampi of females 5xFAD *Pml-/-* compared with 5xFAD (*n* = 3 animals per genotype, p-adj ≤ 0.05, log2(FC) ≥ 0.58). Significantly downregulated genes are shown in blue and upregulated in red. **(B)** Overrepresentation analysis of DEGs for activated and suppressed Gene Ontology (GO) terms in females 5xFAD *Pml-/-* compared with 5xFAD. **(C)** Volcano plot of differentially expressed genes (DEGs) in hippocampi of males 5xFAD *Pml-/-* compared with 5xFAD (*n* = = 3 animals per genotype, p-adj ≤ 0.05, log2(FC) ≥ 0.58). Significantly downregulated genes are shown in blue and upregulated in red. **(D)**Overrepresentation analysis of DEGs for activated and suppressed Gene Ontology (GO) terms in males 5xFAD *Pml-/-* compared with 5xFAD. **(E)** Scatter plot for deferentially expressed genes between 5xFAD *Pml-/-* females and males highlighting common significant genes in both sexes. **(F)** Heatmap of z-score-transformed expression levels of genes related to immune response in female and male hippocampi of 5xFAD and 5xFAD *Pml-/-* mice. (*n* = 3 females and *n* = 3 males). Each row represents a gene, and each column represents an individual mouse sample. **(G)** Heatmap of z-score-transformed expression levels of disease associated microglia (DAM) genes in female and male hippocampi of 5xFAD and 5xFAD *Pml-/-*mice. (*n* = 3 females and *n* = 3 males). Each row represents a gene, and each column represents an individual mouse sample.

Figure 7

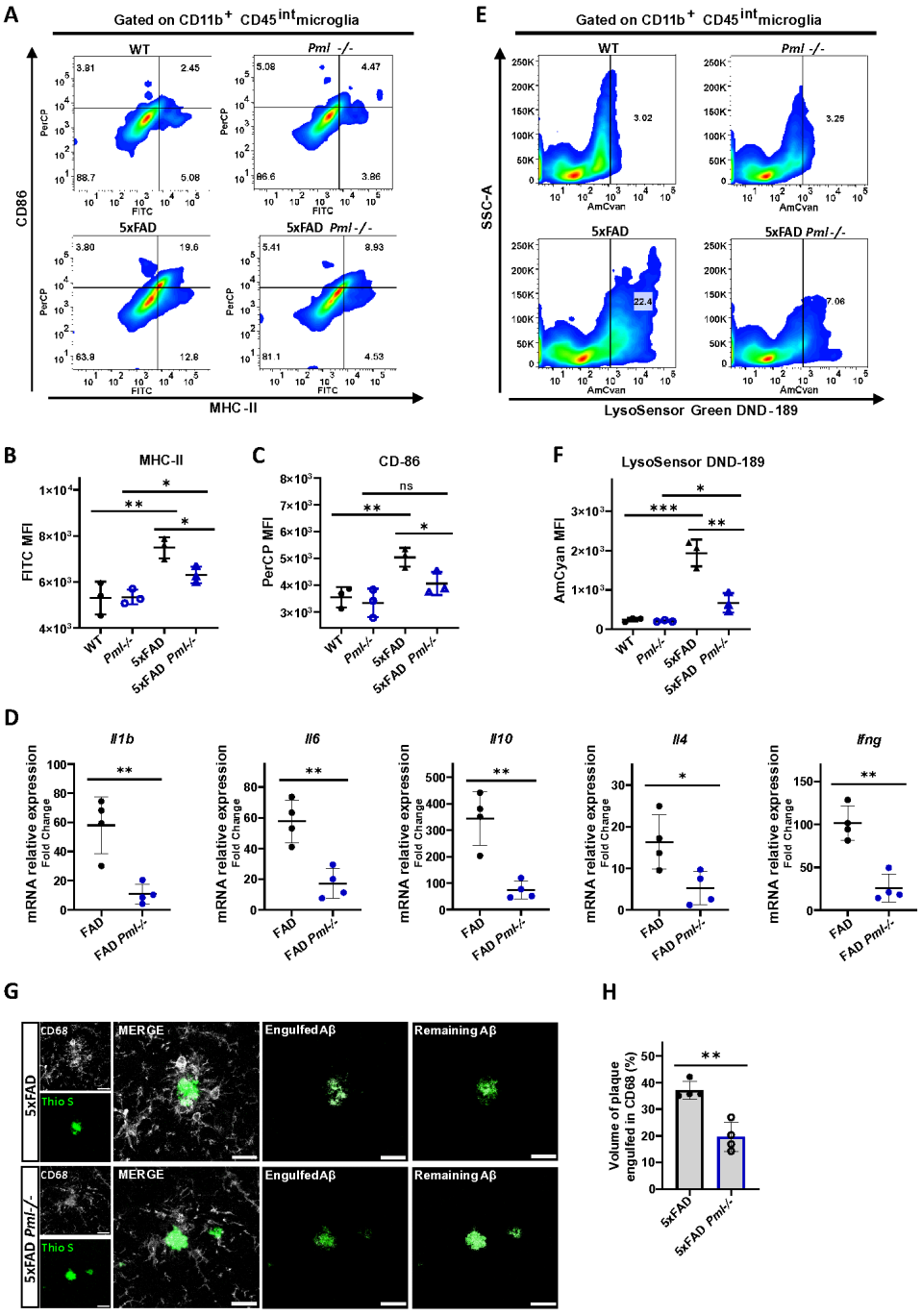


Figure 7

PML promotes microglial immune competence for efficient Aβ plaque clearance.

(A) Flow cytometry analysis of Percoll-isolated microglia from WT, *Pml-/-*, 5xFAD and 5xFAD *Pml-/-* 6 month old mice gated as $CD11b^{+}CD45^{int}$, for MHC-II and CD86 expression. Microglia represent the $CD11b^{+}CD45^{int}$ population. **(B)** Quantification of MHC-II-positive populations. The graph shows the

respective MFIs. (*n*=3 animals per genotype, *p<0.0269, ** p=0.0072; unpaired t-test). **(C)** Quantification of CD86-positive populations. The graph shows the respective MFIs. (*n*=3 animals per genotype, *p=0.0378, ** p=0.0080; unpaired t-test). **(D)** RT-qPCR analysis for pro-inflammatory and anti-inflammatory markers in FACs-sorted microglia from WT, *Pml-/-*, 5xFAD and 5xFAD *Pml-/-* 6 month old mice. (*n*=4 animals per genotype, *p=0.0277, ** p<0.0039; unpaired t-test). **(E)** Flow cytometry analysis of Percoll-isolated microglia from WT, *Pml-/-*, 5xFAD and 5xFAD *Pml-/-* 6 month old mice, for LysoSensor DND-189 staining. Microglia represent the $CD11b^{+}CD45^{int}$ population. **(F)** Quantification of LysoSensor DND-189 staining. The graph shows the respective MFIs. (*n*=3 animals per genotype, *p=0.0325, ** p=0.0065, ***p=0.0008; unpaired t-test). **(G)** Immunofluorescence staining of ThioS+ Aβ plaques (green) and CD68+ phagolysosomes (gray) in 6 months old 5xFAD and 5xFAD *Pml-/-* mice. Aβ volume colocalized within the CD68 volume is shown as a separate channel (yellow). Representative confocal images are shown. Scale bar: 20μm. (H) Quantification of Aβ plaque volume engulfed in CD68 volume. 15 plaques per section with 4 sections per mouse were analyzed (n = 4, all males, **p=0.0016; unpaired t-test). Graphs show mean values ± S.D.

Figure 8

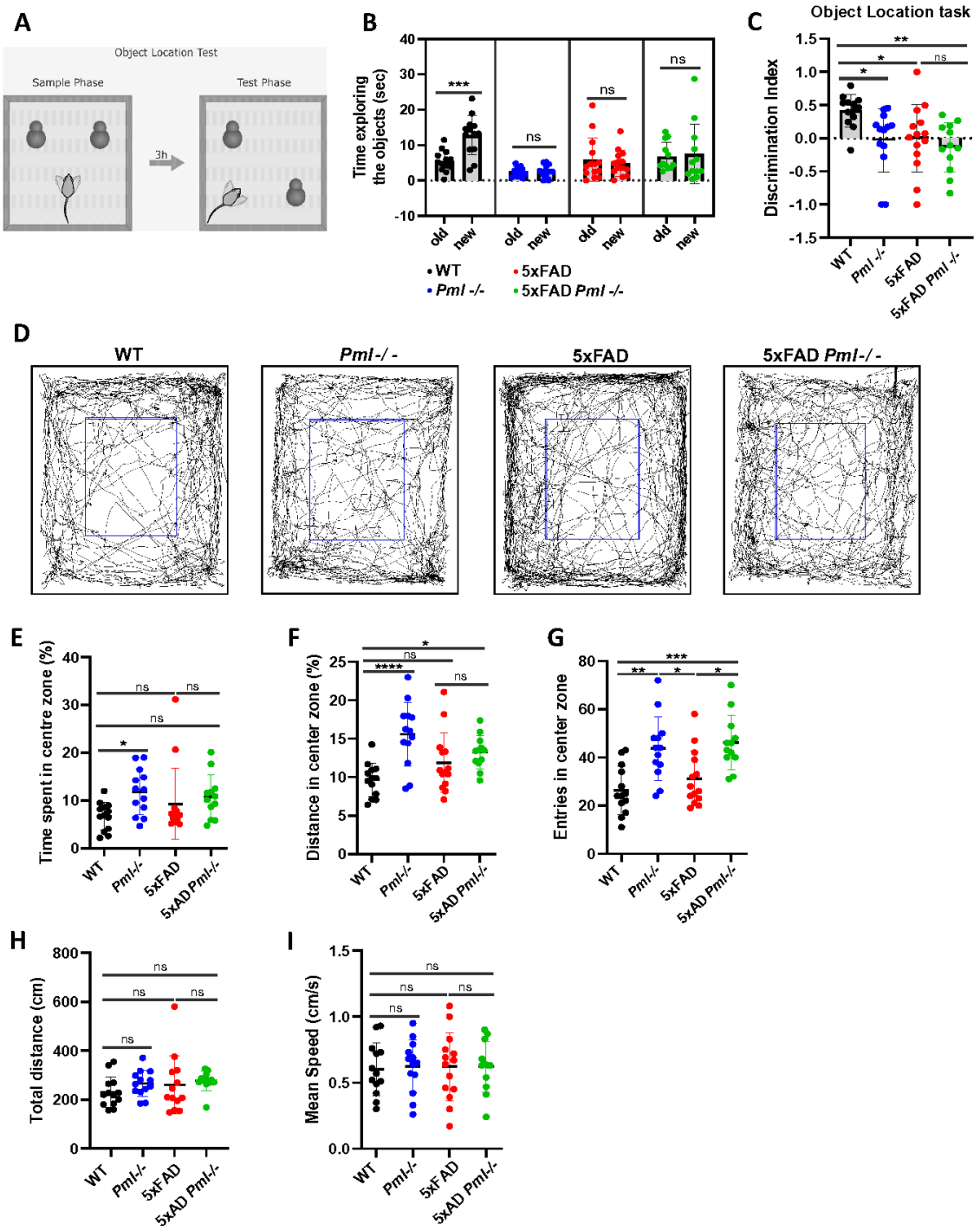


Figure 8

PML depletion exacerbates cognitive deficits and hyperactivity phenotypes in 5xFAD mice.

(A) Schematic representation of the Object Location (OL) task to assess the spatial memory of mice. **(B)** Graph showing the time spent exploring the object's old and new locations, of WT, *Pml-/-*, 5xFAD and 5xFAD *Pml-/-*6 month old mice, in the OL task, (***p=0.0003, unpaired t-test). **(C)** Graph showing the

discrimination index of the OL task of WT, *Pml-/-*, 5xFAD and 5xFAD *Pml-/-* 6 month old mice (*n*=13 WT, *n*=13 *Pml-/-*, *n*=14 5xFAD, *n*=12 5xFAD *Pml-/-*, females and males, *p=0.0252, *p=0.0350, **p=0.0055; one-way ANOVA, Bonferroni's multiple comparison test). **(D)**Representative traces of mouse path in Open-Field test (OFT). The blue box shows the center zone. **(E)** Graph shows quantification of time spent in center zone (%), (*p=0.0482), **(F)** distance traveled in the center zone (%), (*p=0.025, ****p< 0.0001), **(G)** entries in the center zone, (*p=0.0441 for *Pml -/-* vs. 5xFAD, *p=0.0121 for 5xFAD vs. 5xFAD *Pml -/-*, **p=0023, ***p< 0.0006), **(H)** total distance traveled (cm), and **(I)** mean speed (cm/s) in the OFT. Graphs show mean values ± S.D(*n*=13 WT, *n*=13 *Pml-/-*, *n*=14 5xFAD, *n*=12 5xFAD *Pml-/-*, females and males, one-way ANOVA, Bonferroni's multiple comparison test).

Supplementary Files

This is a list of supplementary files associated with this preprint. Click to download.

- TableS5Discordantgenes5xFADPMLKObetweenfemalesandmales.xlsx
- TableS4Hippocampaltranscriptomicanalysis.xlsx
- Spanouetal2026Supplementaryfile1.zip